PHOTOTHERMAL CO_2 REFORMING OF CH_4 BY CONCENTRATED SUNLIGHT

A Thesis

by

JACOB DAVID TRZASKOS

Submitted to the Office of Graduate and Professional Studies of
Texas A&M University
in partial fulfillment of the requirements for the degree of

MASTER OF SCIENCE

Chair of Committee,	Ying Li
Committee Members,	Zhengdong Cheng
	Andrea Strzelec
Head of Department,	Andreas Polycarpou

May 2017

Major Subject: Mechanical Engineering

ABSTRACT

Anthropogenic greenhouse gas emissions have reached record-high concentration levels. These gases are known to affect global temperature. It is crucial to investigate methods of anthropogenic greenhouse gas reduction. Currently, combustion of fossil fuels is the primary cause of human-produced greenhouse gases. While methods are being investigated to replace or modify these combustion systems, this will only impact future greenhouse gas production. In order to reduce concentrations of these gases currently in the atmosphere, chemical reforming is needed. This study will investigate the effect of concentrated solar on the dry reforming of methane with carbon dioxide by synthesizing a suitable catalyst and testing within a custom experimental setup. Non-conventional Hydro-Thermal Synthesis was used for the catalyst. X-ray Diffraction, Ultraviolet-visible Spectroscopy, and Scanning Electron Microscope experiments were used to characterize the catalyst. Additionally, Platinum, Ultraviolet Deposition, and *In Situ* reduction were used to enhance the catalyst. Results from the study show reduced Pt coated $AgNbO_3$ produce inferior levels of product gases compared to more conventionally used catalysts. Stability was enhanced by post fabrication treatments. Additional treatments are needed to enhance carbon removal to prevent rapid degradation.

ACKNOWLEDGEMENTS

I would like to thank my committee chair, Dr. Li, and my committee members, Dr. Cheng, and Dr. Strzelec, for their input and advice during my research. Without constant input, counseling, and direction, this task could not have been accomplished.

I also express my gratitude to Huilei Zhao, our head laboratory assistant. I greatly appreciate the constant assistance I required due to my primary lack of experience in a chemical laboratory setting.

This process would be impossible without the loving support of my family. Thank you for your constant encouragements. I love you all.

Lastly, I want to thank Sofía Carolina Ruiz for all her support throughout the course of my graduate research. Without you, I could not have made it this far. From the bottom of my heart, thank you.

CONTRIBUTORS AND FUNDING SOURCES

This work was supervised by a thesis committee consisting of Professor Strzelec of the Department of Mechanical Engineering and Professor Cheng of the Department of Chemical Engineering.

All other work conducted for the thesis was completed by the student independently.

Graduate study was supported by a fellowship from Texas A&M University and funding by the National Science Foundation under Grant Number 1548091.

NOMENCLATURE

$AgNbO_3$	Silver Niobate
Ar	Argon
C	Celsius
CFCs	Chlorofluorocarbons
CH_4	Methane
CH_x	Methane Decomposition
CO	Carbon Monoxide
CO_2	Carbon Dioxide
CO_x	Carbon Dioxide Dissociation
DI	De-Ionized
DRM	Dry Reforming of Methane
DRS	Diffuse Reflectance Spectra
EM	Electromagnetic (Spectrum)
FID	Flame Ionization Detector
g	grams
GC	Gas Chromatograph
GHGs	Greenhouse Gases
GWP	Global Warming Potential
He	Helium
hrs	hours

H_2	Diatomic Hydrogen
H_2O	Water
ID	Inner Diameter
IR	Infrared
K	Kelvin
MB	Methylene Blue
MFC	Mass Flow Controller
µm	micrometer
mg	milligram
mins	minutes
mL	milliliter
N_2	Diatomic Nitrogen
OD	Outer Diameter
O_2	Diatomic Oxygen
Pt	Platinum
SEM	Scanning Electron Microscope
TCD	Thermal Conductivity Detector
TiO_2	Titanium Dioxide
UV-Vis	Ultraviolet – Visible Spectra
UV	Ultraviolet
λ	wavelength
wt%	weight percent

XRD	X-ray Diffraction Spectra

TABLE OF CONTENTS

Page

ABSTRACT ii

ACKNOWLEDGEMENTS iii

CONTRIBUTORS AND FUNDING SOURCES iv

NOMENCLATURE v

TABLE OF CONTENTS viii

LIST OF FIGURES x

LIST OF TABLES xv

1. INTRODUCTION AND LITERATURE REVIEW 1

    1.1 Greenhouse Gases 1
    1.2 Dry Reforming of Methane 3
    1.3 Alternative Energy Source: Solar 6
    1.4 Catalysts 6
    1.5 Research Objective 8

2. REACTOR DESIGN AND VALIDATION 9

    2.1 Reactor Design 9

3. MATERIAL SYNTHESIS AND CHARACTERIZATION 21

    3.1 Synthesis Method 21
      3.1.1 Hydrothermal Synthesis 21
      3.1.2 Calcination 21
      3.1.3 Photodeposition 22
      3.1.4 *In Situ* H_2 Reduction 22
    3.2 Characterization Methods 22
      3.2.1 X-ray Powder Diffraction 22
      3.2.2 Scanning Electron Microscope 23
      3.2.3 Ultraviolet-Visible & Diffuse Reflectance Spectroscopy 23

4. EXPERIMENTAL PROCEDURES… 24

4.1 Catalytic Dispersion....24
4.2 Dry Reforming of Methane....26

5. RESULTS AND DISCUSSIONS....27

5.1 Characterization Results....27
5.1.1 X-ray Diffraction....27
5.1.2 Scanning Electron Microscope....28
5.1.3 Ultra Violet Spectroscopy & Diffuse Reflectance Spectra....30
5.2 Experimentation Results....33
5.2.1 Reduced 0.2 wt% Pt-$AgNbO_3$....33
5.2.2 Reduced 0.2 wt% Pt-TiO_2 500ºC....34
5.2.3 Reduced 0.2 wt% Pt-TiO_2 600ºC....36
5.3 Results Comparison....38
5.3.1 $AgNbO_3/TiO_2$....38
5.3.2 TiO_2 500ºC/600ºC....38

6. CONCLUSIONS....39

6.1 Summary....39
6.2 Future Work....40

REFERENCES....41

APPENDIX A: PHOTOGRAPHS OF EQUIPMENT SETUP....44

APPENDIX B: MODULAR OPTICS ENCLOSURE AND FILTERS....47

APPENDIX C: CONCENTRATED SOLAR PROJECTION....50

APPENDIX D: PHOTO INTENSITY CHANGE WITH AND WITHOUT LENS....51

APPENDIX E: QUARTZ FRIT DESIGN....53

APPENDIX F: PART FAILURES....54

APPENDIX G: IN SITU REDUCED PT-$AGNBO_3$ EXPERIMENT 1: TESTS 1, 2 AND 3....57

LIST OF FIGURES

Page

Figure 1. Electromagnetic radiation with spectral intensity from 200 to 2500 nm, showing absorption in outer atmosphere and at sea level. Reprinted from [4] 2

Figure 2. Methane Decomposition into CH_x and H_x species, reprinted from [16]. Decomposition shown describes full break down into constituent elements 4

Figure 3. Carbon Dioxide Dissociation into CO_x, C_x and O_x species, reprinted from [16]. Dissociation shown describes full break down into constituent elements 5

Figure 4. ABO_3 Orthorhombic Perovskite structure, reprinted from [13]. The unit cell is cubic with a BCC structure, which repeats to form the larger orthorhombic crystalline lattice 7

Figure 5. Dry Reforming of Methane test equipment schematic 9

Figure 6. Top-down view of the ScienceTech 200-1K lamp housing with MOE's, which housed refractive optics. In MOE 1 the chamber is empty with the exception of a hexagonal prism that aids in focusing the beam. MOE 2 has several refractive optics as well as placements for additional lenses and filters to alter the spectrum and intensity of the light 11

Figure 7. Isometric view of triagonal base plate (X-Y axis) and perpendicular bulb (Z axis). Three set screws were adjusted at the back of the lamp housing to alter the X-Y-Z orientation of the bulb. Depending on location, the projected light could be focused and adjusted for intensity 12

Figure 8. Spectral intensities of Bulb 2 and Bulb 3. Both bulbs were installed and calibrated in-house. Bulb 2 was calibrated at 160W, while Bulb 3 was calibrated at 184W. At their respective times of calibration, these were the minimum power outputs available from the power supply. It was during the calibration of Bulb 3 that power discrepancies became more frequent and pronounced 13

Figure 9A. ATS 3210 Split Tube Furnace with reaction chamber. A 22mm ID by 490mm quartz tube was used as the chamber for the reaction. Couplings with polymer O-rings created seals on each end preventing air from entering the chamber.....14

Figure 9B. Closed view of split tube furnace. From this angle the full conical opening is visible. The solar concentrator is pressed flush against this opening. Note the flow of gas is left to right as indicated by the arrows. Also, fans were used to cool the couplings to prevent deformation of the O-rings.....15

Figure 10. Arrangement of gas cylinders and MFCs. Hydrogen and Argon gas can be seen on either side of the reaction gas (CO_2 / CH_4 / Ar Bal). In front of the cylinders are the three MFCs, each one assigned to their respective gases.....17

Figure 11A. Shimadzu GC-2010 Plus Gas Chromatograph front view. Supply gases for the operation of the GC can be seen to the right. The gas input and exit (vent) are attached to the lower left corner of the GC.....20

Figure 11B. Shimadzu GC-2010 Plus Gas Chromatograph rear view. On the left, the gases needed for the reaction (Air, Argon, Hydrogen, and Helium) can be seen. The gas exit (vent) and input lines can be seen to the right of the GC.....20

Figure 12. Whatman Quartz Fiber Paper with a 22mm cut-out placed on top of quartz frit.....24

Figure 13. Clean and Unclean frit. Contamination from experimental testing can infiltrate the porosity of the frit and reside there until the next test. Cleaning the frit by high temperature baking is a temporary solution.....25

Figure 14A. XRD result of first successful silver niobate (batch #8). This result was compared with results from literature to determine if the correct crystal structure had been fabricated. Successful fabrication was completed on 1/28/16.....27

Figure 14B. XRD results with various pH values from Chang, H. et al, reprinted from [10]. Scans of $pH \neq 3$ indicate additional peaks of Nb_2O_5 and Ag_2O present within the crystalline phase.....28

Figure 15A. SEM images of the silver niobate produced in-house. The scan shows the cubic microstructure with an average size less than 1 μm.....29

Figure 15B. SEM image of silver niobate from Chang, H. et al, reprinted from [10]. The cubic microstructure was characteristic of the hydrothermal synthesis, which is more desirable for catalytic reactions.....29

Figure 16A. $AgNbO_3$ pre and post calcination UV-Vis absorption spectra. Peak absorption shifts forward slightly closer to 400 nm. The sample was calcined at 700°C for 3 hrs before the UV-Vis characterization was completed.....30

Figure 16B. UV-Vis absorption spectra from Li, G., et al, reprinted from [14]. Included here are $AgNbO_3$ samples as well as La promoted samples. The point of interest here is the $AgNbO_3$ absorption curve with peak absorption slightly before 400 nm.....31

Figure 17. Diffuse Reflectance Spectra for calcined and uncalcined $AgNbO_3$. Based on the recorded data, the band gap shifted slightly higher for the calcined sample. $AgNbO_3$ typically has a band gap of 2.86 eV [14].....32

Figure 18. Averaged data of Experiment 1, Averaged DRM tests 1, 2 and 3. 20 mg Pt-$AgNbO_3$, Reduced *In Situ* with 5 mL/min H_2 and 45 mL/min Ar at 500°C for 1 hr, exposed to 10 mL/min of 10% CO_2 / CH_4 / Ar gas at a reaction temperature of 800°C. Photothermal energy supplied was 1000W.....33

Figure 19. Averaged data of Experiment 1, Averaged DRM tests 1, 2 and 3. 20 mg Pt-$AgNbO_3$, Reduced *In Situ* with 5 mL/min H_2 and 45 mL/min Ar at 500°C for 1 hr, exposed to 10 mL/min of 10% CO_2 / CH_4 / Ar gas at a reaction temperature of 800°C. Photothermal energy supplied was 1000W.....35

Figure 20. DRM test with 20 mg Pt-TiO_2, Reduced *In Situ* with 5 mL/min H_2 and 45 mL/min Ar at 500°C for 1 hr, exposed to 10 mL/min of 10% CO_2 / 10 % CH_4 / Ar gas at a synergistic reaction temperature of 600°C.....37

Figure 21A. Isometric view of experimental setup. Equipment components are listed as numbers 1 through 4. Item number 1 being the GC, 2 the Continuous Solar Concentrator, 3 the Split Tube Furnace, and 4 the MFCs. From this view, the spatial setup of the experiment can be appreciated.....44

Figure 21B. Side view of experimental setup (excluding GC). Equipment Components are listed as numbers 2 through 4 as the GC is not pictured here. From this view, the gas cylinders for the DRM can be seen.....45

Figure 22. Rear view of experimental setup. Pictured here are the Solar Concentrator, MFCs, and Solar Power Supply. Note the holes at the base of the Lamp Housing. These are intake holes for the cooling air.....46

Figure 23. MOE 1 and 2 close up.....47

Figure 24. Concave bulb housing with cathode. In the center of the concave base, the bulb is positioned. By adjusting the depth of the bulb (Z-axis only) the intensity will be directly affected.....48

Figure 25. Transmittance Intensity and UV Filters for MOE 1. These filters allow the transmittance of the inscribed level of light intensity. Last is the UV filter which allows light with a wavelength up to 400 nm.....49

Figure 26A. Hexagonal projection of point intensity supplied by ScienceTech. Indications of intensity values were not included in literature supplied.....50

Figure 26B. Photograph of concentrated solar hexagonal projection on target. Photograph was included in literature supplied by ScienceTech.....50

Figure 27A. Spectral Irradiance plots of Bulb #2 with Quartz lens in place. Light spectrum is full UV-IR ranging from 250-950nm. Loss of intensity due to lens is approximately 5%.....51

Figure 27B. Spectral Irradiance plots of Bulb #2 without Quartz lens.....52

Figure 28. Schematic of Quartz tube and frit to be used as a catalyst substrate. Large quartz tube used for the reaction chamber was 22mm interior diameter and 25mm outer diameter. The small quartz tube which was fuzed with the frit had an inner diameter of 19mm and an outer diameter of 22mm. See Figure 13 for clean vs contaminated frit.....53

Figure 29. Splayed high amperage wire used inside lamp housing. Lamp arrived with broken wire inside. A replacement was ordered and took several weeks to arrive.....54

Figure 30A. Bulb #1 failure. After running at 1600W for several hours, lamp suddenly failed. Fracture near the cathode allowed xenon gas to escape. A replacement bulb was ordered and took 3 months to arrive.....55

Figure 30B. Bulb #2 failure. After running at 1600W for several hours, bulb suddenly failed. Crack near cathode was similar to Bulb #1 failure. However charring of interior region between nodes indicates a combustion process. A replacement bulb was ordered and took 1 month to arrive.....56

Figure 31A. Pt-$AgNbO_3$, Reduced DRM Test 2 with 20 mg Pt-$AgNbO_3$, Reduced *In Situ* with 5 mL/min H_2 and 45 mL/min Ar at 500°C for 1 hr, exposed to 10 mL/min of 10% CO_2 / 10% CH_4 / Ar gas at a reaction temperature of 800°C.....57

Figure 31B. Pt-$AgNbO_3$, Reduced DRM Test 1 with 20 mg Pt-$AgNbO_3$, Reduced *In Situ* with 5 mL/min H_2 and 45 mL/min Ar at 500°C for 1 hr, exposed to 10 mL/min of 10% CO_2 / 10% CH_4 / Ar gas at a reaction temperature of 800°C.....58

Figure 31C. Pt-$AgNbO_3$, Reduced DRM Test 3 with 20 mg Pt-$AgNbO_3$, Reduced *In Situ* with 5 mL/min H_2 and 45 mL/min Ar at 500°C for 1 hr, exposed to 10 mL/min of 10% CO_2 / 10% CH_4 / Ar gas at a reaction temperature of 800°C. This differs from previous tests and the quantities of production are ~3x higher than the other two tests.....59

LIST OF TABLES

Page

Table 1. Calculated and Reference K-Factors for Omega FMA 5400/5500 Series MFCs. All controllers were measured with respect to Nitrogen gas, the K-factors used for Nitrogen are 1.....15

1. INTRODUCTION AND LITERATURE REVIEW

1.1 Greenhouse Gases

Civilization has developed an increasing need for the consumption of fossil fuels. Combusting these fuels serves as a power source to drive industry, yet it leaves behind ever-increasing amounts of byproduct gases. Typically, gases are vented to open atmosphere with little to no filtration or re-capture systems. This has led to a drastic increase of atmospheric concentrations of what are commonly called 'greenhouse gases' [1, 2]. Greenhouse gas emissions have been shown to correlate with an increased global temperature. Anthropogenic (human activity related) activity has only increased these gas concentrations in the atmosphere. In recent years, this increase has brought new attention to addressing the issue of atmospheric greenhouse gase concentrations [3].

A greenhouse gas is a gaseous compound, residing in any layer of the atmosphere that contributes to the greenhouse effect [4]. In this region, Electromagnetic (EM) Radiation from the Sun is absorbed by these gases either as they enter the atmosphere or they absorb IR radiation that the earth emits as a blackbody radiator. A graph of these wavelengths can be seen in **Figure 1**. These gases trap the radiation and redirect it back to the earth [4]. Greenhouse gases are commonly 'trace gases,' or gases that make up less than 1% of the atmospheric composition, but can still impact the climate [1].

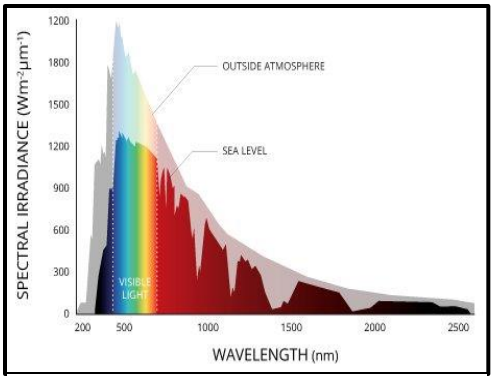

Figure 1. Electromagnetic radiation with spectral intensity from 200 to 2500 nm, showing absorption in outer atmosphere and at sea level, Reprinted from [4].

Targets of recent investigations center on Carbon Dioxide (CO_2), Methane (CH_4), Water Vapor (H_2O), and ChloroFluroCarbons (CFC's). Much investigative effort has been directed to the first two as they are direct combustion byproducts of fuel usage. Their ability to absorb and send back heat is called the Global Warming Potential (GWP). The GWP is a function of both radiative forcing and residence time [1]. Some gases have a shorter residence time, meaning they will decompose or dissociate spontaneously in the atmosphere. CO_2 has a residence time of roughly 230 yrs while CH_4 has a residence time of 14.4 yrs [1]. On a human time scale, CH_4 will break down into gases that either do not contribute to the greenhouse effect or have a lower GWP value. CO_2, however, is a longer term problem. Yet CH_4, despite its much shorter life span, has a GWP of nearly 25 times that of CO_2 [1]. CO_2 GWP is standardized to 1 and all other GHGs (greenhouse gases) are compared it.

Studies have been done and have confirmed an increasing anthropogenic atmospheric GHG concentration and global temperature correlation [2]. It then follows that tremendous amounts of time and effort have been invested into systematic reduction of these gases in the atmosphere. It is from a global objective that this project derives its meaning.

1.2 Dry Reforming of Methane

A process or system of processes that can reduce the amount of CO_2 & CH_4 in atmosphere is desirable. Several options exist such as carbon capture or increased biological involvement. One method that is of extreme interest is the reforming of CH_4 with CO_2. This method uses an energy source to reform CH_4 and CO_2 into H_2 and CO, commonly known as synthesis gas or "syn gas" [5]. It is especially interesting, as its products can be used for several chemical processes to create long chain hydrocarbons or produce diatomic hydrogen gas [6]. The reaction also produces different ratios of CO:H_2 which are ideal for use in the Fischer-Tropsch reactions [6]. Typically, the process of reforming CH_4 is utilized with steam [21]. While this is a viable option, it is not always feasible for remote processing where water isn't available. Also, with the abundance of CH_4 in sources like natural gas, biodegradation of organic sources, and natural processes, a CH_4 reforming system that can be used more broadly without water is highly desirable [2].

The CO_2 reduction of CH_4, or the Dry Reforming of Methane (DRM), is endothermic. Practically, this reaction requires high temperatures. One study indicates that the temperature of reforming is between 700°C - 950°C [9]. Others indicate the range

could be as great as 500°C - 1100°C depending on the catalyst [5,7,8,20]. This implies the reaction will consume high amounts of energy to complete the DRM. Conventionally, this energy has been supplied by high temperature sources. Most of these high temperature sources utilize, either directly or indirectly, energy from fossil fuels. This presents a problem, as it is counterproductive to the reduction of GHGs.

Previous research has examined the reaction mechanisms investigating the reforming of CO_2 with CH_4. **Figure 2** shows the decomposition of CH_4 into a series of CH_x species. The H^-species are adsorbed by the metal and decompose on the surface [2].

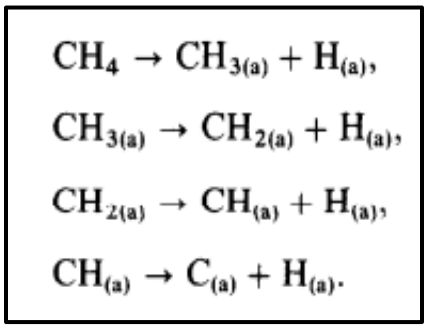

Figure 2. Methane Decomposition into CH_x and H_x species, reprinted from [16]. Decomposition shown describes full break down into constituent elements

However, the most important issue is the resulting carbon from the decomposition, which can take several forms. The carbon deposits can be in the form of atomic, amorphous, bulk, vermicular, and/or crystalline [15]. One study found the endothermic decomposition led to deposited carbon reacting with oxygen species of hydroxyl groups

to form CO [2]. Thus, a key area of catalyst design must account for the prevention of carbon formation and the recombination of carbon with other reactants present.

Characteristically, the presence of solid carbon from the methane decomposition is limited, especially when adsorbed onto a noble metal catalyst. However, carbon adverse reactions are exacerbated in the presence of free radical oxygen, which can be primarily supplied by CO_2 dissociation [15]. In general, CO_2 dissociation takes place on a transition metal [2]. **Figure 3** displays the dissociation process for Carbon Dioxide. And while CH_4 decomposition can be enhanced by adsorbed oxygen, CO_2 dissociation is promoted by adsorbed hydrogen and possibly other CH_x residue species [15]. Other reactions such as hydroxyl group formation, the reverse water gas shift, and water vapor formation can all spontaneously occur during reaction conditions [2], [15].

$$CO_2 \rightarrow CO_{(a)} + O_{(a)},$$

$$CO_{(a)} \rightarrow C_{(a)} + O_{(a)}.$$

Figure 3. Carbon Dioxide Dissociation into CO_x, C_x, and O_x species, reprinted from [16]. Dissociation shown describes full break down into constituent

1.3 Alternative Energy Source: Solar

As mentioned previously, the DRM reaction is endothermic. It is common for this temperature to be achieved via thermal energy from a combustion process. However, this implies the process requires energy which can be from a non-thermal source.

A highly sought-after potential source is solar radiation. The radiation that is incident upon the ground has a wavelength ranging from UV to IR (100 - 1,000,000 nm) [4]. Common intensity levels for these wavelengths can be seen in **Figure 1.** Studies have been done to show how a solar-activated catalyst can utilize energy to complete a DRM reaction [7]. These studies and experiments utilize high temperature and concentrated solar energy coupled with a catalyst to complete the reaction. While the effects from temperature are known, the photothermal effect is a mostly ignored phenomenon that can contribute to the reaction.

1.3 Catalysts

It is one focus of this work to find a suitable catalyst for this reaction that will make the process more efficient energy-wise as well as utilize a frequently neglected energy source: the sun. Catalysts have many factors that can affect their efficiency such as; substrate material, microstructure, porosity, coating, layer thickness, crystallite geometry, and coating technique [7]. One of the most difficult aspects of the design will be the restriction of carbon formation. Temperatures above 1000K with CO_2:CH_4 ratios above unity will avoid the thermodynamic conditions that foster carbon deposition [2]. Additionally, literature is at odds about the nature of carbon formation. Some indicates carbon formation is from the decomposition of CH_4 or the disproportionation of CO_2.

Literature suggests that at high temperatures, thermodynamic conditions are unfavorable for carbon retention of the catalyst [9]. Other sources indicate adding impurities to the metal, such as sulfur in a process that is called sulfur poisoning, can also make unfavorable conditions for carbon deposition [6]. Regardless of the method, this is an important aspect of design that must be addressed.

A suitable catalyst needs to be stable at high temperatures, able to withstand degradation, easy to fabricate, potentially able to self-clean, prevent carbon formation, and modifiable with the coating of metal ions. Perovskites with the structure ABO_3, were chosen since they are oxide semiconductors.

In the ABO_3 structure, seen in **Figure 4**, B ions may be catalytically active 3d, 4d, or 5d transition metals [12].

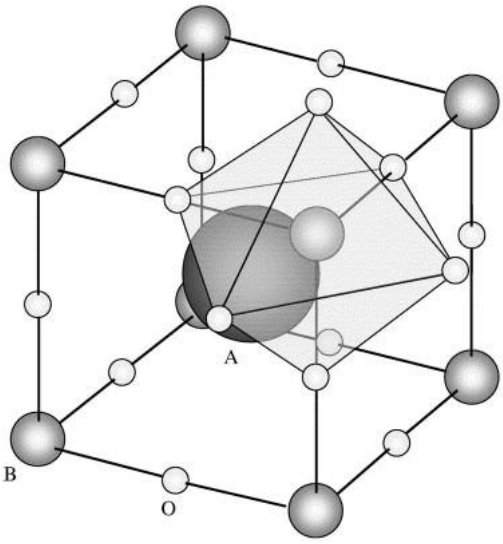

Figure 4. ABO_3 Orthorhombic Perovskite structure, reprinted from [13]. The unit cell is cubic with a BCC structure which repeats to form the larger orthorhombic crystalline lattice.

The A ions which fit into dodecahedral interstices are typically large rare-earth, alkaline-earth, alkali, or other large ions [11, 12]. Since this arrangement of ions is variable, perovskite structure offers several key advantages. These are; a wide variety of composition and constituent elements, well-characterized bulk structure, widely variable valency with stoichiometry and vacancy, and there are large volumes of information of the physical properties of the structure [13]. Specifically, the valency and vacancy controls have great influence on the catalytic effects of the material [13]. For this experiment, Silver Niobate ($AgNbO_3$) was chosen due to its desirable band gap of 2.8 eV, an absorption range of 200 nm - 550 nm, fine-tunable catalytic properties during synthesis, direct and controllable synthesis via hydrothermal method, and notably its stability at high temperatures [10, 18, 19].

Samples of silver niobate were fabricated via hydrothermal synthesis, inspired by the procedure outlined in Chang, Haibo et al [10]. Pure $AgNbO_3$ was first synthesized, calcined, and finally platinum coated using UV photodeposition. Reduced coated samples were done *In Situ* with diatomic hydrogen.

1.5 Research Objective

It is the focus of this study to investigate catalytic synthesis and characterization, reactor assembly and validation, and the photothermal effect in the DRM reaction.

2. REACTOR DESIGN AND VALIDATION

2.1 Reactor Design

To conduct the DRM reaction experiments, a system was designed, assembled, and validated. The reactor was designed to meet several requirements. It was able to house a high temperature DRM reaction with the ability to introduce controlled photonic or thermal energy either individually or synergistically. This reaction supplied controlled flows of specific gases for the DRM reaction. Finally, it was able to continuously sample and analyze the byproducts of the reaction in real time.

The proposed setup, outlined in the NSF grant[1], was separated into four sections of equipment; Gas Chromatograph, Continuous Solar Concentrator, Tube Furnace with Reaction Chamber, and Mass Flow Controllers. The schematic used for the study can be seen **Figure 5**.

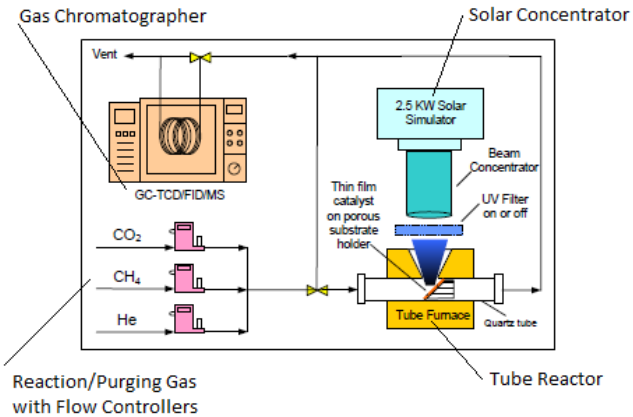

Figure 5. Dry Reforming of Methane test equipment schematic.

All components of the design will be discussed in further detail in the following sections. Photographs of the actual setup can be seen in *Appendix A.* While previous work has been done in concentrated solar dry reforming, this study conducted a small scale reactor setup without the use of large parabolic mirrors [7,8]. It also attempted using a more stable energy source in the form of a continuously concentrated solar lamp.

Thus the reactor design required an adequate solar concentrator capable of providing a stable and continuous output of broad spectrum radiation. A custom arc lamp setup from ScienceTech was utilized. Their ScienceTech 200-1K lamp housing with custom modular optics enclosures (MOE's) were used to provide controllable continuous concentrated broad spectrum solar radiation. The lamp was designed to use a 1.6 KW bulb which was typically a high-pressure Xenon arc lamp bulb. The bulb was also provided by ScienceTech. These arc bulbs provided UV-IR spectrum of irradiation. Power was supplied by an AC power supply which converted the signal to DC and altered the current while supplying constant voltage. In order to operate the lamp, the power supply current was adjusted resulting in a change in wattage. The maximum power setting available was 1600 W. The solar concentrator can be seen in **Figure 6.** A magnified image of this setup can be seen in *Appendix B.* The lamp radiation was concentrated using a concave mirror into a series of lenses and a hexagonal prism to collect and focus the light into a set area.

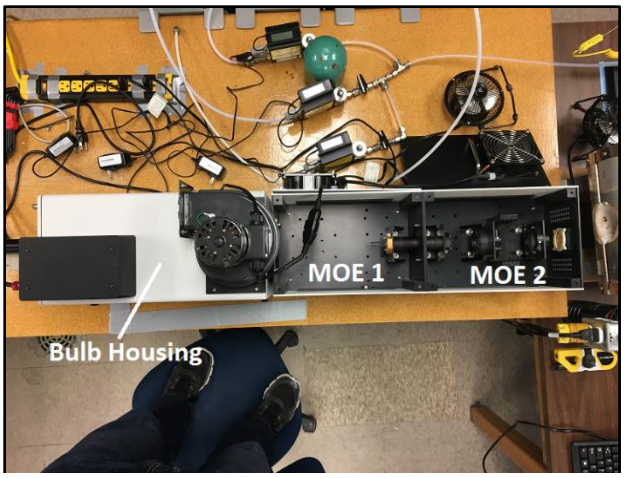

Figure 6. Top down view of the ScienceTech 200-1K lamp housing with MOE's which housed refractive optics. In MOE 1 the chamber is empty with the exception of a hexagonal prism which aids in focusing the beam. MOE 2 has several refractive optics as well as placements for additional lenses and filters to alter the spectrum and intensity of the light.

However, the focal point of the light beam needed to be tuned by adjusting the triagonal baseplate which supports the anode end of the bulb. This base plate can be seen in **Figure 7.** The plate was set in the X-Y plane and was adjusted by tuning each set screw individually at the back of the lamp housing. As the screw turned, the baseplate shifted and resulted in a change of light intensity. Adjustment was complete when intensity was maximized. As the plate was adjusted, the bulb moved along the Z-axis which was parallel to the direction of the light. The further along the positive Z-axis, away from the back of the concentrator, the greater the intensity. An image of the projected radiation area, both theoretical and actual, can be seen in *Appendix C.*

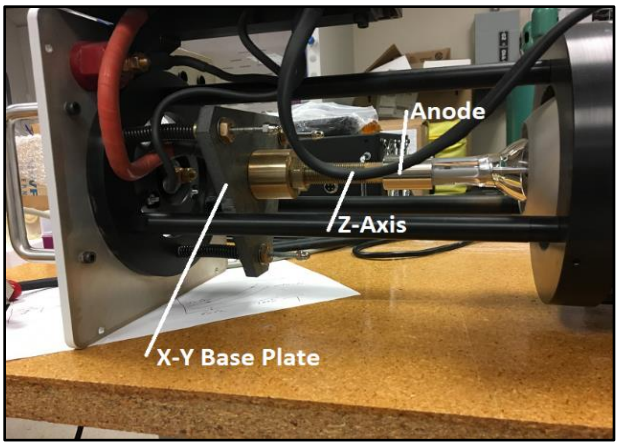

Figure 7. Isometric view of triagonal base plate (X-Y axis) and perpendicular bulb (Z axis). Three set screws were adjusted at the back of the lamp housing to alter the X-Y-Z orientation of the bulb. Depending on location, the projected light could be focused and adjusted for intensity.

In order to quantify the intensity and focus of the beam, an optical sensor was used to measure these qualities of the light. Real-time output from a ILT950 Spectroradiometer from InternationalLight displayed intensity vs wavelength data, which was recorded. Finally, the data was output to Microsoft Excel 2010. The spectral plot of bulbs 2 and 3, can be seen below. **Figure 8** displays the spectral intensities of the second bulb compared to the third as both were installed and calibrated in-house. Bulb 2 was calibrated at 160 W while Bulb 3 was calibrated at 184W. The difference is due to the power supply. On the day of Bulb 3 calibration, the lowest attainable power was 184W. However, despite the higher power, the overall intensity is lower. This suggests the methods used for calibration may not be robust enough, or there are variations of power with different bulbs.

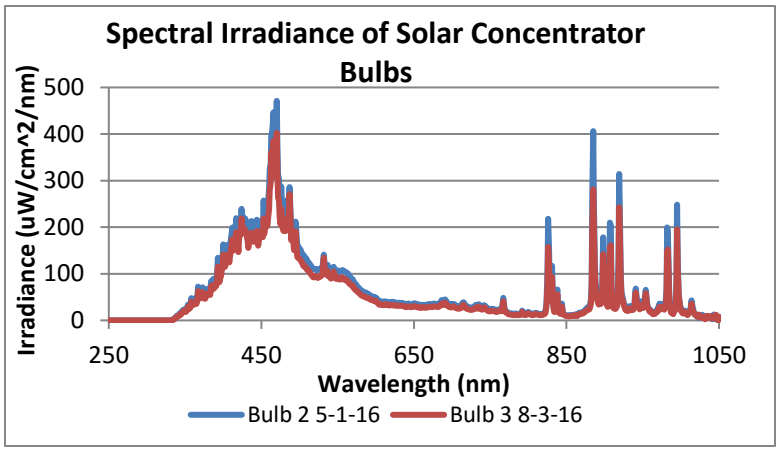

Figure 8. Spectral intensities of Bulb 2 and Bulb 3. Both bulbs were installed and calibrated in-house. Bulb 2 was calibrated at 160W while Bulb 3 was calibrated at 184W. At their respective times of calibration, these were the minimum power outputs available from the power supply. It was during the calibration of Bulb 3 that power discrepancies became more frequent and pronounced.

An important thing to note is the focal length. Due to dimensional constraints of the furnace and concentrator, the target irradiated with light was a distance of 130 mm from the face of the concentrator. The system was designed to have a focal length of 100 mm from the front face of the concentrator. Advice given from ScienceTech was to achieve a distance as close to 100mm as possible and calibrate at low power. For the purposes of calibration and testing, a target distance was fixed at 130mm.

By achieving the minimum target distance, the solar concentrator was placed tangent to the tube furnace. This enabled the high velocity air, used to cool the lamp, to escape from the opening of the solar concentrator and enter the tube furnace. This cooled the tube furnace, limiting the maximum temperature it could achieve. The solution was to

use a thin plane of cut-out quartz glass, 40mm in diameter, to cover the opening. It was held in place by a custom 3-D printed holder. This setup can be seen in *Appendix C.*

The last issue was the reduction of solar intensity due to the plane of quartz glass. Tests were conducted using the same optical sensor from International Light as listed previously. It was found to reduce the overall intensity of the light by approximately 5%. An image of the intensity plots with and without lens can be found in *Appendix D.*

As mentioned, DRM reactions take place at elevated temperatures. Therefore, a furnace with sufficient insulation and heating ability was used. It also housed the reaction chamber and allowed for photo-irradiation. A split tube furnace was supplied by Applied Test Systems (ATS). **Figure 9A** shows the 3210 Series furnace with a conical cutaway perpendicular to the axial direction allowing solar radiation to be introduced to the reaction chamber.

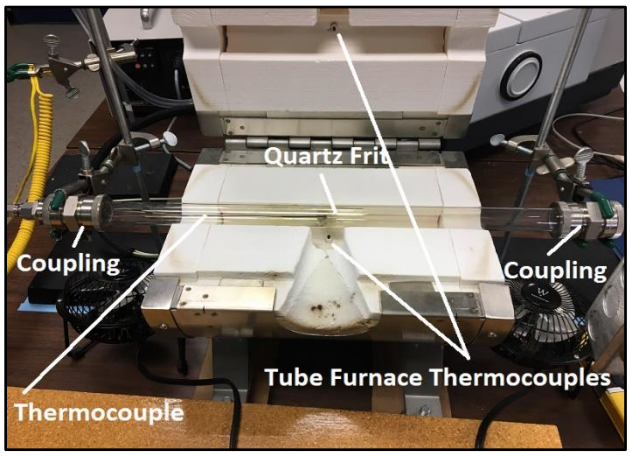

Figure 9A**.** ATS 3210 Split Tube Furnace with reaction chamber. A 22mm ID by 490 mm quartz tube was used as the reaction chamber for the reaction. Couplings with polymer O-rings created seals on each end preventing air from entering the chamber.

Embedded in the walls of the furnace were two K-type thermocouples, which allowed the system to monitor temperature and provide feedback to the power supply. This exterior thermocouple was later changed to a custom Omega 558 mm (22 inch) K-Type thermocouple, which was inserted into the reaction chamber and incident upon the reaction surface. This aided in reducing temperature lag.

The setup of the tube furnace and reaction chamber can be seen in **Figure 9B**, which shows the direction of gas flow as well as the cooling fans. Their main function was to cool the couplings to prevent O-ring deformation.

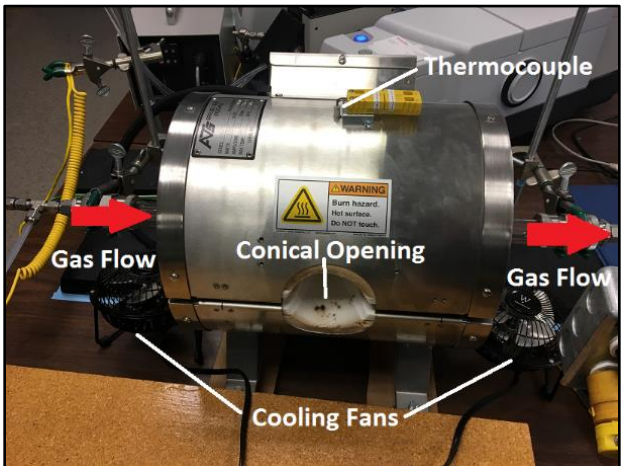

Figure 9B**.** Closed view of split tube furnace. From this angle the full conical opening was visible. The solar concentrator was pressed flush against this opening. Note the flow of gas was left to right as indicated by the arrows. Also, fans were used to cool the couplings to prevent deformation of the O-rings.

Within the furnace was a 22mm ID by 558mm long quartz tube that housed the reaction. Either end of the tube was sealed with quick disconnect couplings with polymer O-rings to prevent gas leakage. Fabricated from a meter-long quartz tube, the reaction chamber was cut to length with a diamond grind wheel and fire polished on the ends to prevent fracture and cracking.

Inside the tube was a custom thermocouple that was incident upon the reaction surface. At the left end, the thermocouple was inserted through a Swagelok reducing union and was incident upon the powdered catalyst. It was suspended on Whatman Quartz grade Filter paper that was cut into a 20mm x 14mm oval. Location of the suspended catalyst was adjusted such that it was in the path of the solar irradiation within the conical opening.

The reactor used controllers to restrict the gas flow being introduced to the chamber. All controllers were Omega FMA5400/5500 series MFCs. In total, three controllers were used with the flow range settings as follows: 500 mL/min, 50 mL/min, and 10 mL/min. The 500 mL/min controller was used for the purging gas, Ultra High Purity, Argon from AirGas. The 50 mL/min controller was used for the reaction gas cylinder, which was also an Airgas CO_2 / CH_4 / Ar Balance sample. The 10 mL/min flow controller was used for the Airgas Compressed Hydrogen. **Figure 10** displays the setup of cylinders and MFCs.

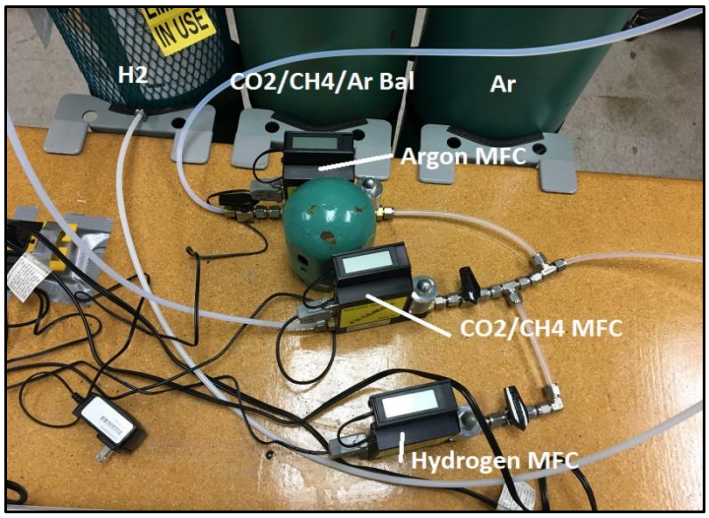

Figure 10. Arrangement of gas cylinders and MFCs. Hydrogen and Argon gas can be seen on either side of the reaction gas (CO_2 / CH_4 / Ar Bal). Infront of the cylinders are the three MFCs, each one assigned to their respective gas.

Controllers were calibrated using K-factor conversions verified by a Gilian Gilibrator 2 model 850190-1 with a Gilian Low Flow Cell. K-factors for Argon (1.205) and Hydrogen (1.35) were obtained from the FMA 5400/5500 Users Guide. Calculated K-factors were obtained by measuring flow through the Gilian Low Flow Cell for the desired gas and flow rate. Values for calculated K-factors can be seen in **Table 1**.

	Ar	Ar	$CO_2/CH_4/AR$	H_2
Set Flow	100 mL/min	45 mL/min	10 mL/min	5 mL/min
Av. Flow (10 Samples)	120.73	68.239	13.771	6.74
K-Factor (Calculated)	1.231	1.516	1.391	1.348
K-Factor (Manual)	1.205	1.205	N/A	1.35
Percent Difference	2.2%	25.8%	N/A	11.8%

Table 1. Calculated and Reference K-Factors for Omega FMA 5400/5500 Series MFCs. All controllers were measured with respect to Nitrogen gas, this K-factors used for Nitrogen are 1**.**

Observed differences between calculated K-factors and values given in the manual suggested an issue with calibration of the MFCs. Since the in-house equipment has been used for several years, the need for factory adjustment is likely. Therefore, the values obtained from the Gilian Low Flow Cell should be considered more reliable as the equipment is not frequently used and still valid within its calibration certificate.

Gases were required for purging, *In Situ* reduction, and the DRM reaction. The gases used are as follows: UHP Argon (99.999%), CO_2/CH_4 Mixture (10.0% each) with Ar balance, and Compressed Hydrogen, all of which were supplied by AirGas.

Purging was done with the UHP Argon, as it is inert and is not read in the GC. Flow rates for the Argon were 100 mL/min and 45 mL/min. The high flow was used for purging the reaction chamber, and the low flow was used for *In Situ* reduction. It had a volume of 848.45 mL, which affected the purging time required. A flow of 100 mL/min could theoretically purge the chamber in as little as 8.5 mins, but purge times were often

as long as 30 mins. This was due to issues of residual oxygen and water vapor present inside the reaction chamber, which needed to be minimized before utilizing the GC.

Gas composition identification was done using a gas chromatograph. It consisted of a moving phase (inert carrier gas) and a stationary phase (liquid or polymer on inert support), which interacted. When the unknown gas reacts with the column walls, the compound elutes (extraction of one material from another by solvent washing) at different times. These times are referred to as retention times and are unique to each chemical element or compound. After the columns, the gas may pass through additional detectors. For this setup, two detectors were used. A Shimadzu GC-2010 Plus Gas Chromatograph was obtained for the laboratory. **Figures 11A and 11B** show the front and back setup of the GC.

The GC used both FID and TCD detectors for gas analysis. This system used UHP Argon to act as a carrier gas. Helium was also used as a carrier gas for the FID. The FID used combustion with hydrogen to detect the chemical species present in the sample, while the TCD used thermal conductivity. In total, four gases (compressed air, hydrogen, argon, and helium) were used to operate the GC.

Figure 11A. Shimadzu GC-2010 Plus Gas Chromatograph front view. Supply gases for the operation of the GC can be seen to the right. The gas input and exit (vent) are attached to the lower left corner of the GC.

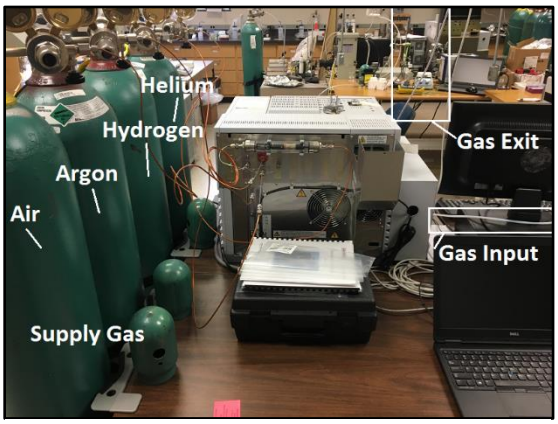

Figure 11B. Shimadzu GC-2010 Plus Gas Chromatograph rear view. On the left, the gases needed for the reaction (Air, Argon, Hydrogen, and Helium) can be seen. The gas exit (vent) and input lines can be seen to the right of the GC.

3. MATERIAL SYNTHESIS AND CHARACTERIZATION

3.1 Synthesis Methods

Synthesis for $AgNbO_3$ was done using the hydrothermal method. Calcination was done at high temperature for several hours. Samples were coated with Pt via photodeposition then reduced *In Situ*.

3.1.1 Hydrothermal Synthesis

Inspired by the procedure outlined in Chang, Haibo et al [10], precursors NH_4HF_2, Ag_2O, and Nb_2O_5, were measured in samples of 0.3433g, 0.927g, and 1.08g respectively. These were mixed by magnetic stirring into a 60 mL beaker of DI water for 10 mins at low speed before being placed in a 100 mL Teflon-lined stainless steel autoclave. Though the literature called for a temperature of 240°C for 24 hours, the in-house autoclave could only safely be used at 200°C [10]. Samples were collected by centrifugal separation and were washed a minimum of 3 times. Washing was done with additional DI water and repeated centrifugal separation. They were dried in a 60°C oven.

3.1.2 Calcination

Post synthesis sample sizes of $AgNbO_3$ ranged from 200-300 mg of catalyst. The catalyst was placed in a ceramic cup inside the furnace and the temperature was set to 700°C at a rate of 10°C/min with soak time of 3 hrs. When finished, the sample was removed, cooled, and ground with a mortar and pestle. The ground calcined sample was then placed in a labeled container for storage.

3.1.3 Photodeposition

The addition of Pt to $AgNbO_3$, photodeposition was used to degrade H_2PtCl_6 by UV light. 100mg of $AgNbO_3$ was added to 50 mL of DI water in a 100 mL beaker with 1 mL ethanol. The calculated amount of Pt was added based on weight percent. Samples of 0.2 wt%. were synthesized by 841.9µL of 0.5 mg/mL concentration H_2PtCl_6 added to the DI water. It was then stirred magnetically and placed under a UV lamp for 3 hrs. After, samples were washed with DI water, collected by centrifugal separation, and placed in the drying oven overnight.

3.1.4 In-Situ H_2 Reduction

Once the catalyst was placed into the reaction chamber, it was reduced with a 10% H_2, 90% Ar. Flow rates were 5 mL/min and 45 mL/min for H_2 and Ar respectively. Reduction temperature inside the chamber was 500°C which took place for 1 hr. Finally, the chamber was flushed with Ar at 100 mL/min for approximately 15 mins.

3.2 Characterization Methods

3.2.1 X-ray Powder Diffraction

X-ray Powder Diffraction is used for the identification of the sample's crystalline phase and structure. XRD scans were completed at the Materials Development and Characterization Center using a Bruker D8 Cu-tube sealed X-ray scanner. After synthesizing $AgNbO_3$, the plot in **Figure 14A** was achieved. It was compared with **Figure 14B.** Both can be seen Chapter 5.

3.2.2 Scanning Electron Microscope

SEM imagery was done at the Materials and Characterization Facility, MFC, with the JEOL JSM-7500F ultra high resolution field emission scanning electron microscope. In Chapter 5, **Figure 15A** shows the SEM image from in house fabrication which can be compared with the results of the surface morphology from literature in **Figure 15B**

3.2.3 Ultraviolet-Visible & Diffuse Reflectance Spectroscopy

$AgNbO_3$ has strong absorption around ~400 nm, placing it in the short wavelength section of the visible spectrum with a low band gap of 2.8 eV [14]. The results show in **Figures 16A & B** in Chapter 5 show the in-house scans and literature references respectively.

Results of the scan can be found in Chapter 5 in **Figure 17**

4. EXPERIMENTAL PROCEDURES

4.1 Catalytic Dispersion

One method for dispersion involved dissolving the powdered catalyst into a beaker of 200-300 µL of DI water before utilizing a pipette to disperse the catalyst. The mixture is dropped onto an oval quartz fiber paper cut-out of 20mm x 14mm. An image of this can be seen in **Figure 12.** The coated fiber is placed in an oven at 60°C for a minimum of 1.5 hours.

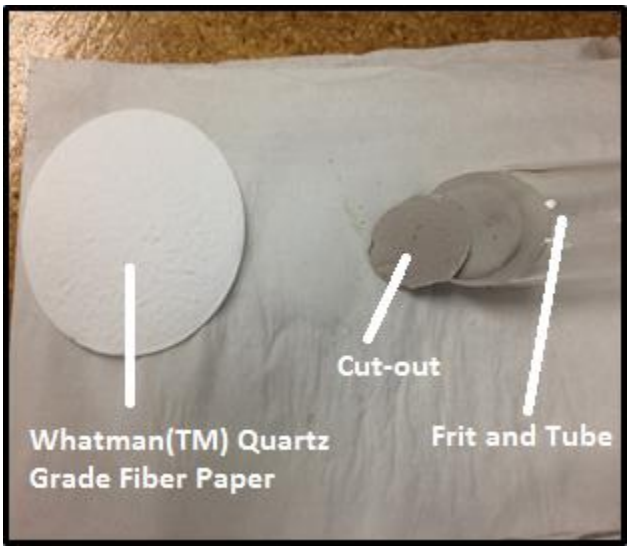

Figure 12. Whatman™ Quartz Fiber Paper with 22mm cut out placed on top of quartz frit.

Another method of dispersion used spreading of sample on top of a dampened fiber cut-out. By wetting the fiber cut-out with ~100µL of DI water, the powdered catalyst

adhered to the fibers. Both methods of dispersion allow for the catalyst to seep into the quartz frit substrate below the fiber paper.

The frit was a 30mm diameter, 150-200µm porosity quartz substrate used to support the doped fiber paper. A tube of 19mmID 22mOD was cut at a 45º angle and the frit was cut down to size to fit. It was fused to the tube at high temperature. Full fabrication of the frits were done at the Glass Shop in the Chemistry Building. The design of the frit can be seen in *Appendix E.*

Figure 13 shows the difference between a clean and contaminated frit. After every test, the fiber containing the catalyst is removed.

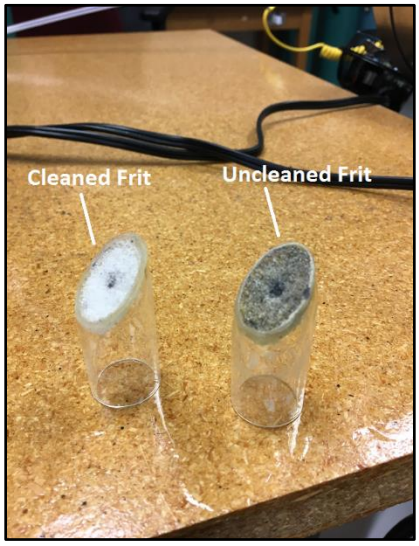

Figure 13. Clean and Unclean frit. Contamination from experimental testing can infiltrate the porosity of the frit and reside there until the next test. Cleaning the frit by high temperature baking is a temporary solution.

A new fiber was used each time, yet the frit was reused. In order to clean the frit, it was placed in an oven at 800°C for 3 hours. This heat treatment can bake off the contaminants and help partially clean the frit. After many uses, it becomes too contaminated to use again and must be replaced.

4.2 Dry Reforming of Methane

Testing procedure for both Pt-$AgNbO_3/TiO_2$ are as follows. Once the sample of either Pt coated $AgNbO_3$ or TiO_2 had been loaded, it was reduced *In Situ*. In these reductions, H_2 was used with Ar. At 10% concentration, 5 mL/min H_2 was mixed with 45 mL/min Ar at 500°C for 1 hr as it passed through the reaction chamber and across the catalyst. Once this process was complete, the chamber was purged with Ar at 100 mL/min for ~ 15 mins. The flow rate of reaction gas was set to 10 mL/min when the purging gas was shut off. Then a test queue was setup to take injections every 15 minutes for a total of 16 samples.

5. RESULTS AND DISCUSSIONS

5.1 Characterization Results

5.1.1 X-ray Diffraction

Figures 14A and 14B display the crystalline structure of the synthesized $AgNbO_3$ compared to literature. Note the scan of ph = 3 and its correlation between the figures.

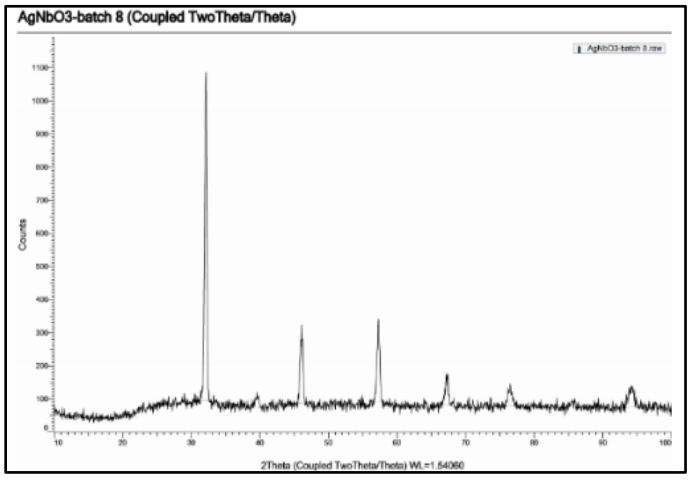

Figure 14A. XRD result of silver niobate batch #8 following the updated instructions. This result is compared with results from literature to determine if the correct crystal structure had been fabricated. Successful fabrication was completed on 1/28/16.

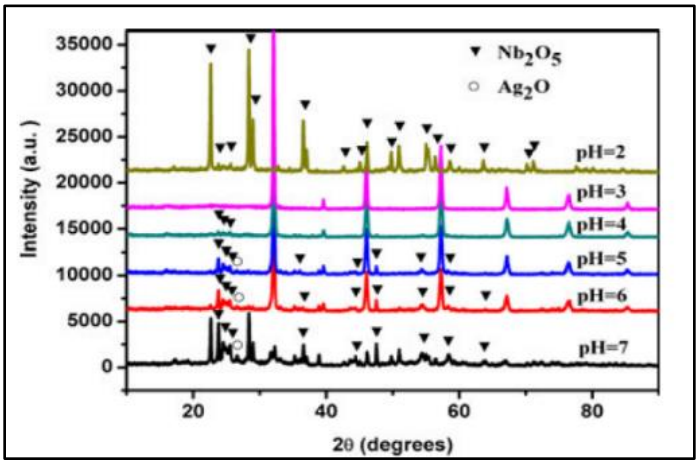

Figure 14B. XRD results with various pH values from Chang, H. et al, reprinted from [10]. Scans of pH ≠ 3 indicate additional peaks of Nb_2O_5 and Ag_2O present within the crystalline phase.

The XRD does show the successful phase synthesis of $AgNbO_3$ in **Figure 14A** compared to the pH=3 scan in **Figure 14B**. This is the desirable structure as it shows no trace of precursors Nb_2O_5 or Ag_2O. Thus the crystallographic phase is highly likely to be the same as reported in literature, which is beneficial for reduction reactions. Phase change at higher temperature was limited by calcination and the catalysts own ability to remain stable at elevated temperature.

While XRD is used to determine the phase and crystalline structure, it is only relevant for the unit cell dimensions, meaning it does not identify nanostructures of the particles in the sample. Hence, another method of characterization must be used.

5.1.2 Scanning Electron Microscope

Examining **Figure 15A**, the cubic structure of the perovskite particles matches that of the documented literature. The image in **Figure 15B** is from Chang, Haibo et al

and is used for comparison of the microstructure [10]. Both images show microstructures around or below 1µm in size and generally cubic in nature.

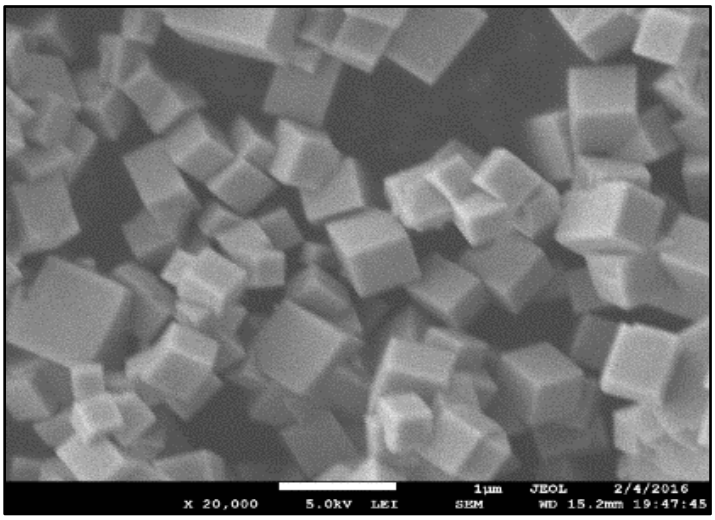

Figure 15A. SEM images of the silver niobate produced in-house. The scan shows the cubic microstructure with an average size less than 1 µm in size.

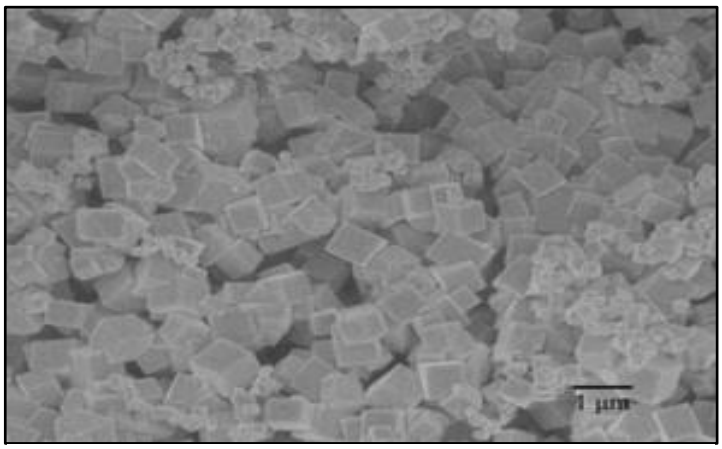

Figure 15B. SEM image of silver niobate from Chang, H. et al, reprinted from [10]. The cubic microstructure is characteristic of the hydrothermal synthesis which is more desirable for catalytic reactions.

The cubic structure of the perovskite particles matches that of the documented literature. Cubic structure is more desirable for the reaction than amorphous particles as they will promote the DRM. From these images and peak graphs we can say with a high degree of certainty that we have successfully synthesized the working catalyst via the hydrothermal method as stated in Chang, Haibo et.al [10]. This catalyst will serve as the basis for the next stage in the development, which is the addition of the promoter.

5.1.3 Ultra Violet Spectroscopy & Diffuse Reflectance Spectra

Figure 16A shows the UV-Vis absorption of pre and post-calcined $AgNbO_3$ samples. Calcined absorption more closely reflects the trend seen in literature as shown in **Figure 16B.** Samples in **Figure 16A** show very different spectral absorption with shifts occurring after calcination. The peak absorption more closely resembles that seen in **Figure 16B** for pure $AgNbO_3$.

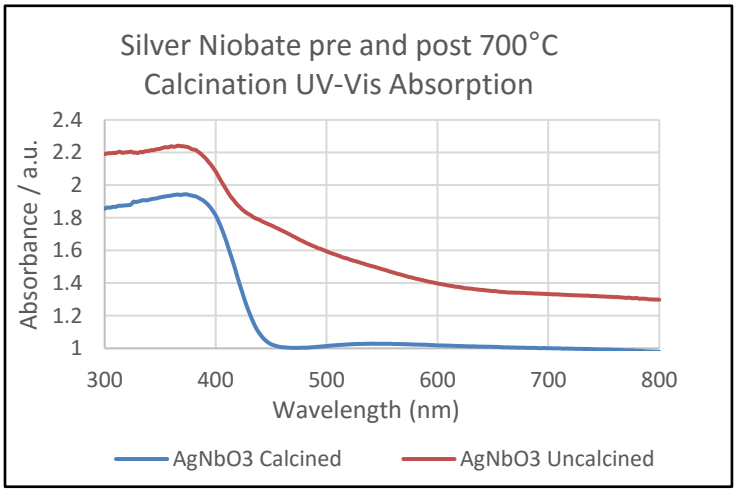

Figure 16A. $AgNbO_3$ pre and post calcination UV-Vis absorption spectra. Peak absorption shifts forward slightly closer to 400 nm. The sample was calcined at 700°C for 3 hrs before the UV-Vis characterization was completed.

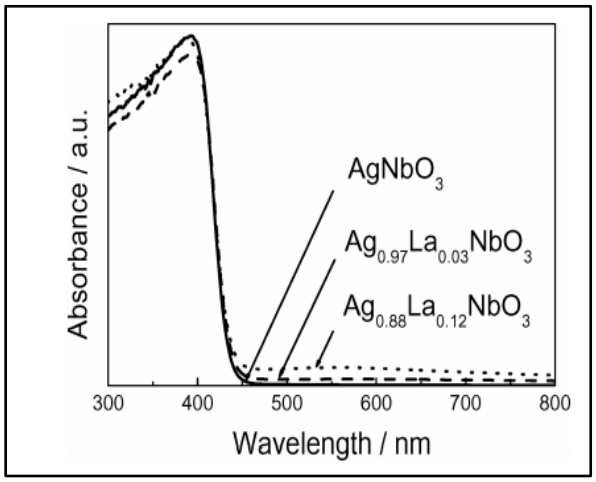

Figure 16B. UV-Vis absorption spectra from Li, G., et al, reprinted from [14]. Included here are $AgNbO_3$ samples as well as La promoted samples. The point of interest here is the $AgNbO_3$ absorption curve with peak absorption slightly before 400 nm.

$AgNbO_3$ has strong absorption around ~400 nm, placing it in the short wavelength section of the visible spectrum with a low band gap of 2.8 eV [14]. Its absorption edge puts it in the visible spectrum. Thus it will use photothermal energy with the potential for wavelength absorption to further promote the DRM.

Calcination shifts the absorption edge, most likely by changes to surface microstructure as well as bulk property changes [17]. It also shifts the main absorption peak closer to the 400nm mark.

UV-Vis diffuse reflectance spectra was used to calculate the band gap for both calcined and uncalcined samples. The results can be seen in **Figure 17**. As shown, the calculated band gap for the samples is high compared to typical reports in literature. Deviations in geometric structure, impurities in the bulk structure, and or microstructure

growth defects could be attributed to this increase. However, it is likely these influences are minimal due to the high correlation of the characterized samples in literature.

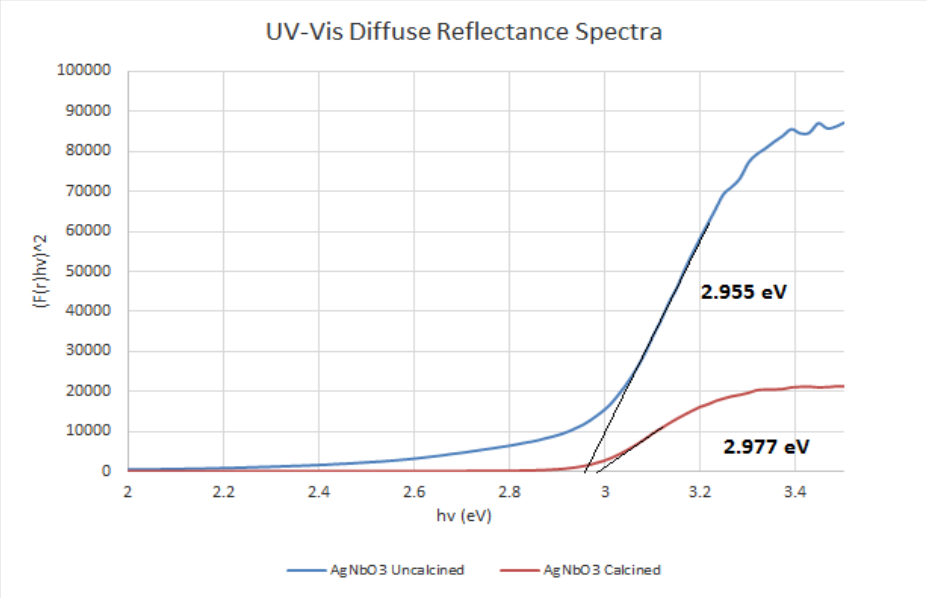

Figure 17. Diffuse Reflectance Spectra for calcined and uncalcined $AgNbO_3$. Based on the recorded data, the band gap shifts slightly higher for the calcined sample. $AgNbO_3$ typically has a band gap of 2.86 eV [14].

5.2 Experimental Results

5.2.1 Reduced 0.2 wt% Pt-$AgNbO_3$

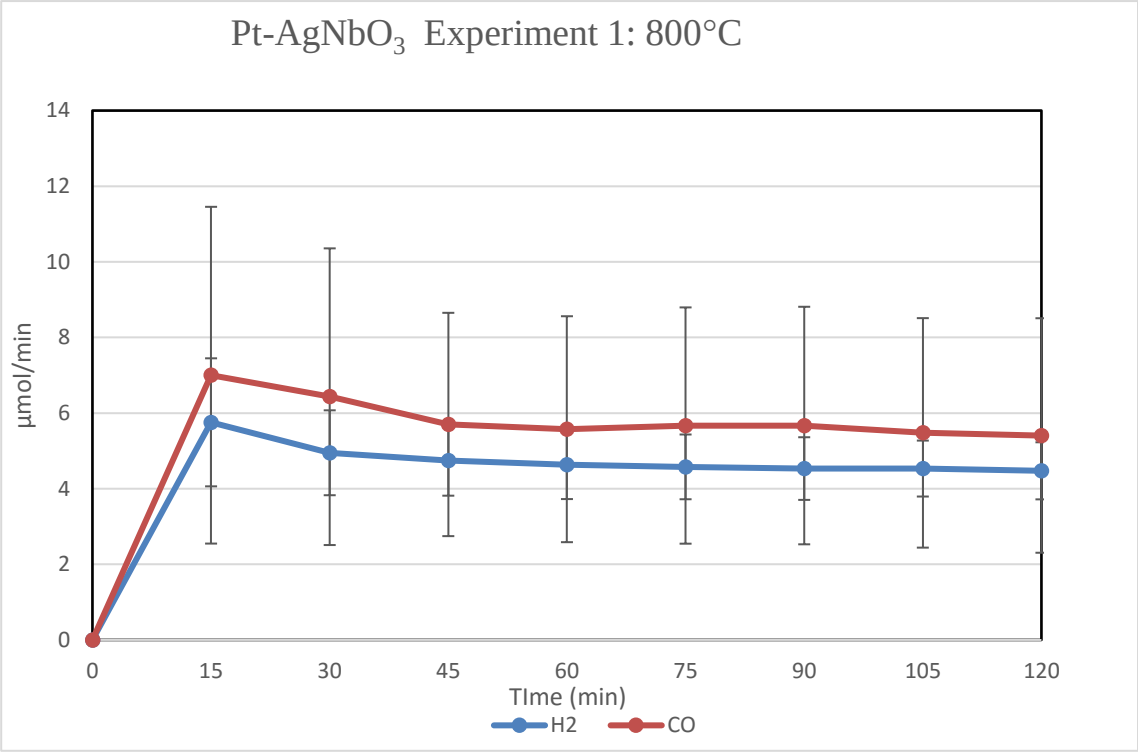

Figure 18. Averaged data of Experiment 1, Averaged DRM tests 1, 2 and 3. 20 mg Pt-$AgNbO_3$, Reduced *In Situ* with 5 mL/min H_2 and 45 mL/min Ar at 500°C for 1 hr, exposed to 10 mL/min of 10% CO_2 / 10% CH_4 / Ar gas at a reaction temperature of 800°C. Photothermal energy supplied was 1000W.

The reaction temperature set to 800°C by supplying 1000W of photothermal energy. The remaining energy required to achieve the 800ºC was supplied by the tube furnace. Ideally, higher photo power would be used yet due to unstable fluctuations in power from the lamp and the destruction of two previous bulbs, the power remained at

1000W. **Figure 18** displays the results of Reduced Pt-$AgNbO_3$ Experiment 1, which consisted of 3 tests. Data was averaged and plotted with error bars.

Production levels initially peak followed by a slight decrease into stabilization. Ratios of H_2 to CO are approximately 0.8. Unity is ideal for the later use of the product gases, yet these results are acceptable. Stabilization is also favorable as this indicates the catalytic production is consistent and deactivation is limited. Based on the number of tests, the variance of the data is noticeable high given the compared levels of production. Ideally given a production of 6µmol/min, it is not desirable to have a deviation of +/- 3µmol/min.

5.2.2 Reduced 0.2 wt% Pt-TiO_2 500ºC

Many catalysts have been investigated for their use in the DRM reaction, perhaps none so much as titanium dioxide (TiO_2). Its stability, easy of synthesis, low cost, proven ability as a catalyst, and widely researched modifications made it a suitable bench mark to compare with this study [5,16,20]. Consequently, an experiment was run to compare the effect TiO_2 in the DRM.

Thus TiO_2, doped with 0.2 wt% Pt and heating it to a synergistic 500°C with the solar concentrator was, tested in the subsequent experiment. 1240W was used due to bulb stability. The remaining energy necessary for the reaction was supplied by the tube furnace. At 1600W intensity fluctuations were noticed. Thus power was reduced to a lower level that was more stable and also corresponded to 250°C. The rest of the energy was supplied by the tube furnace. As seen in **Figure 19**, the results of the test show that the photothermal energy in the reactor setup is sufficient to affect the DRM reaction. The

next step was to test the desired catalyst at a higher reaction temperature with *In Situ* reduction.

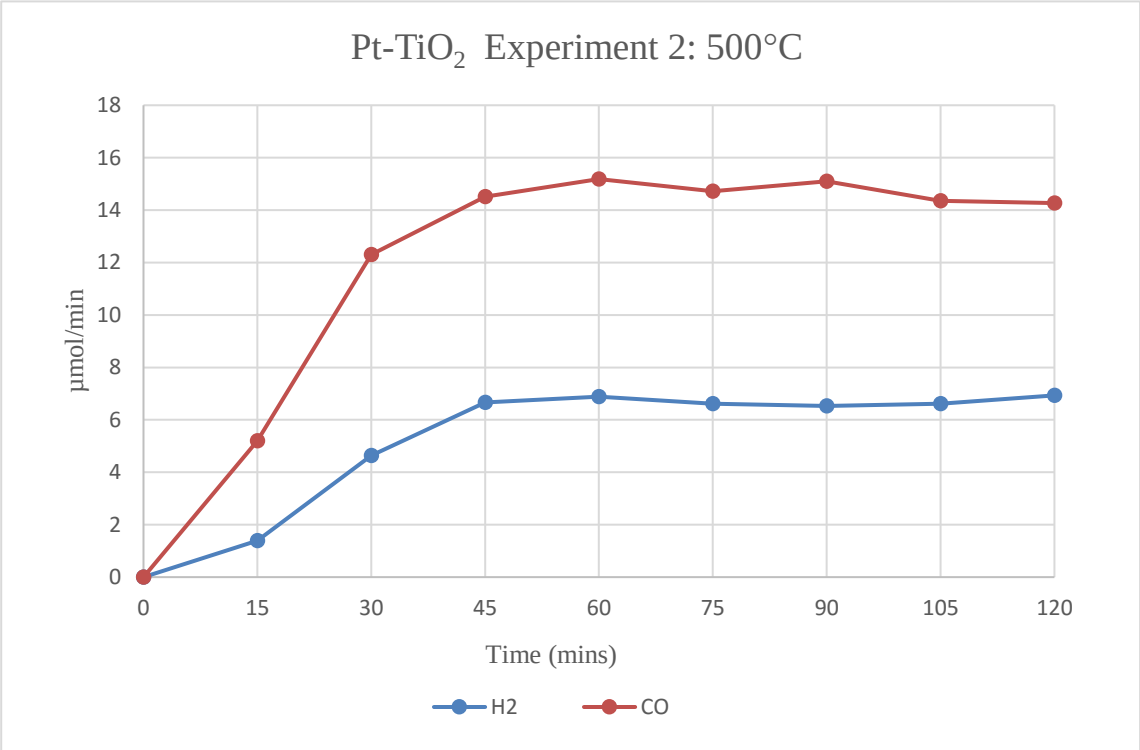

Figure 19. Averaged data of Experiment 1, Averaged DRM tests 1, 2 and 3. 20 mg Pt-$AgNbO_3$, Reduced *In Situ* with 5 mL/min H_2 and 45 mL/min Ar at 500°C for 1 hr, exposed to 10 mL/min of 10% CO_2 / CH_4 / Ar gas at a reaction temperature of 800°C. Photothermal energy supplied was 1000W

The results shown indicate rapid increases in production followed by a stabilization range. The ratio of H_2 to CO is slightly lower than 0.46. Ideally production levels closer to unity are desired. It would be beneficial to enhance the hydrogen evolution to increase the product ratio. Stability suggests the catalyst is able to retard degradation

and promote the reaction for a prolonged period of time as the results were compiled over 2 hrs.

5.2.3 Reduced 0.2 wt% Pt-TiO_2 600ºC

At elevated temperatures, T > 600°C, TiO_2 will begin to phase change from anatase into rutile. Anatase is more desirable than rutile for the catalytic reaction and thus it should not exceed this temperature [22,24]. P25 is a mixture of 80% anatase and 20% rutile TiO_2 commonly used in DRM reactions [24-26]. An experiment was conducted with reduced Pt-TiO_2 in order to determine the effect it has on the DRM. During this time, issues arose with the bulb. Power fluctuations were continuing to produce instabilities in temperature. Therefore the power was reduced significantly to ensure power and temperature stability. **Figure 20** displays the results of this test.

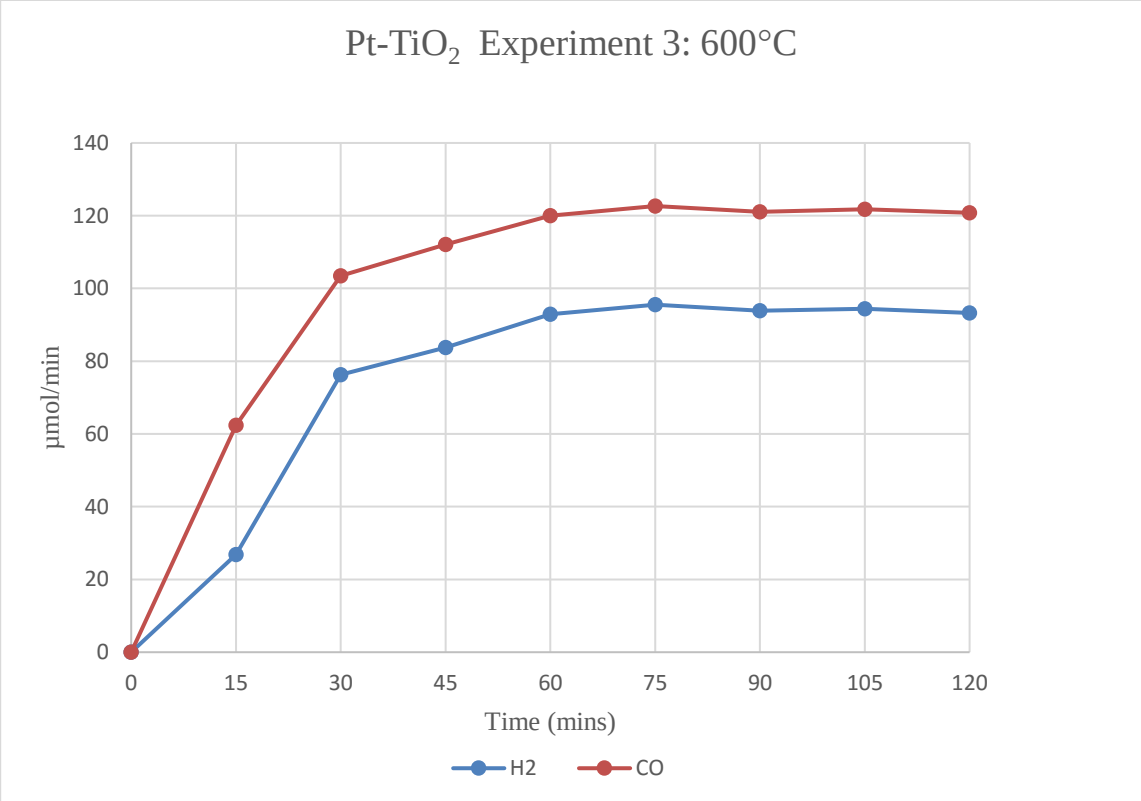

Figure 20. DRM test with 20 mg Pt-TiO_2, Reduced *In Situ* with 5 mL/min H_2 and 45 mL/min Ar at 500°C for 1 hr, exposed to 10 mL/min of 10% CO_2 / 10% CH_4 /Ar gas at a reaction temperature of 600°C.

Results of the test display the drastic increase in concentration of product gases. 600W of photothermal energy was supplied and the remaining required energy was supplied by the tube furnace. The levels of productivity are considerable. Approximately 7-8x as high in level, the reactants are present in much greater levels in this test. The ratio of H_2 to CO are also approximately 0.8 which is close to unity. Again, this is ideally would be as close to unity as possible. However the level of production, coupled with product ratio and stability make these results favorable.

5.3 Results Comparison

5.3.1 $AgNbO_3/TiO_2$

When comparing the results of the $AgNbO_3$ samples to the TiO_2, the levels of production are immediately noticed. TiO_2 produces higher levels of gas at 500ºC and considerably higher levels at 600ºC. The ratios of H_2 to CO are also more favorable in the TiO_2 tests compared to the $AgNbO_3$ tests. In both test groups stability is present with neither showing a distinct advantage other the other. Overall productivity, product ratio and stability are favorable for TiO_2 over $AgNbO_3$.

5.3.2 TiO_2 500ºC/600ºC

The most noticeable difference between the 500ºC and 600ºC tests are the difference in production. Because of the higher reaction temperature, the test with the produced higher levels of gas despite lower photothermal energy. Thus suggests the reaction may be more sensitive to overall reaction temperature. The higher temperature test also displayed slightly more stable production of gases, but this is not definitive. Finally the ratio of H_2 to CO is more desirable for the high temperature reaction. Values for the high temperature reaction are much closer to unity than the lower temperature reaction. In both cases of TiO_2 results are acceptable with the higher temperature test being more desirable.

6. CONCLUSIONS

6.1 Summary

$AgNbO_3$, was successfully synthesized via the hydrothermal method. This synthesis method allowed for precise cubic nanostructures which were preferred to the amorphous nanoglobules which arise from Sol-Gel or Solid State Reactons. The characterization methods of XRD and SEM confirm the successful synthesis and microstructure of $AgNbO_3$.

In order to conduct the dry reforming test, a working design of the equipment was created and implemented. A custom solar concentrator, gas chromatograph, tube furnace with reaction chamber and mass flow controllers were setup as a reactor system. The reactor was validated with a test of 50/50 split of thermal and photothermal energy. It utilized a known catalyst with documented performance in DRM reactions. Results showed the photothermal energy source can promote the DRM reaction.

Testing was done with 0.2 wt% Pt-$AgNbO_3$ and 0.2 wt% Pt-TiO_2 for reference. It utilized *In* Situ reduction and identical catalyst amounts and gas flow rates. This was due to the phase of TiO_2 being unstable above 600°C and the bulb/lamp not being able to achieve a stable power above 600W. Yet despite this lower temperature and power the production for the TiO_2 was more than one full order of magnitude greater.

As of now, no literature exists on the use of $AgNbO_3$ in the dry reforming reaction, thus there is no standard with which to compare. Its effectiveness in this reaction was not

as high as as Pt- TiO_2, which can produce higher levels of product gases at lower temperatures, remain active longer, are easy/easier to produce, and are similar in cost.

6.2 Future Work

Continuation studies into this body of work would be advantageous on several topics. Mainly, the investigation of other metal promoters and interstitial lattice elements which could be used to modify the $AgNbO_3$ structure. Also the investigation of other noble metal promoters aside of Pt could be beneficial. Research has indicated that Ir, Ru, and or Rh can be beneficial [13, 16, 26]. It would also be of benefit to examine concentrations of these additions as they can affect the DRM reaction.

Another main area of investigation would focus on a more desirable photothermal source. During testing, the bulb and power supply showed issues of stability. Also two bulbs were broken due to inability to operate at the maximum power. This suggests that either the bulbs or the power supply are not properly calibrated to ensure functional operation. Thus it would be beneficial to use a higher power and more stable bulb.

The last area of investigation would involve adjusting catalytic concentrations and gas flow rates. Combining different masses with flow rates may affect the DRM reaction. Thus an ideal combination could be found to promote the DRM reaction.

REFERENCES

[1] Lashof, D. A., and D. R. Ahuja. "Relative contributions of greenhouse gas emissions to global warming." *Nature* 344.6266 (1990): 529-531.

[2] Bradford, M. C. J., and M. A. Vannice. "CO_2 reforming of CH_4." *Catalysis Reviews* 41.1 (1999): 1-42. 100101948

[3] Rodhe, H. "A comparison of the contribution of various gases to the greenhouse effect." *Science* 248.4960 (1990): 1217.

[4] Schneider, S. H. "The greenhouse effect: Science and policy." *Science* 243.4892 (1989): 771-781.

[5] Stagg-Williams, S. M., et al. "Metal-support interaction on Pt/ZrO_2 catalysts for the CO_2 reforming of CH_4." *Studies in Surface Science and Catalysis* 130 (2000): 3663-3668.

[6] Rostrupnielsen, J. R., and JH Bak Hansen. "CO_2-reforming of methane over transition metals." *Journal of Catalysis* 144.1 (1993): 38-49.

[7] Muir, J. F., et al. "Solar reforming of methane in a direct absorption catalytic reactor on a parabolic dish: I—Test and analysis." *Solar Energy* 52.6 (1994): 467-477.

[8] Levy, M., et al. "Methane reforming by direct solar irradiation of the catalyst." *Energy* 17.8 (1992): 749-756.

[9] Treacy, D., and J. RH Ross. "The potential of the CO_2 reforming of CH_4 as a method of CO_2 mitigation. A thermodynamic study." *Prepr. Pap.-Am. Chem. Soc., Div. Fuel Chem* 49.1 (2004): 127.

[10] Chang, H., et al. "Hydrothermal syntheses and structural phase transitions of $AgNbO_3$." *Journal of the American Ceramic Society* 95.11 (2012): 3673-3677.

[11] Li, X., and J. Zang. "Facile hydrothermal synthesis of sodium tantalate ($NaTaO_3$) nanocubes and high photocatalytic properties." *The Journal of Physical Chemistry C* 113.45 (2009): 19411-19418.

[12] Voorhoeve, R. J. H., et al. "Perovskite oxides: materials science in catalysis." *Science* 195.4281 (1977): 827-833.

[13] Tanaka, H., and M. Misono. "Advances in designing perovskite catalysts." *Current Opinion in Solid State and Materials Science* 5.5 (2001): 381-387.

[14] Li, G., et al. "Enhanced photocatalytic activity of La-coated $AgNbO_3$ under visible light irradiation." *Dalton Trans.*, 2009, 2423-2427

[15] Edwards, J. H., and A. M. Maitra. "The chemistry of methane reforming with carbon dioxide and its current and potential applications." *Fuel Processing Technology* 42.2-3 (1995): 269-289.

[16] Stagg, S. M., and D. E. Resasco. "Effect of promoters on supported Pt catalysts for CO_2 reforming of CH_4." *Studies in Surface Science and Catalysis* (1998): 813-818.

[17] Al-Fatesh, A. S. A., and A. H. Fakeeha. "Effects of calcination and activation temperature on dry reforming catalysts." *Journal of Saudi Chemical Society* 16.1 (2012): 55-61.

[18] Shu, H., et al. "Structural characterization and photocatalytic activity of $NiO/AgNbO_3$." *Journal of Alloys and Compounds* 496.1 (2010): 633-637.

[19] Wang, C., et al. "Synthesis and characterization of $AgBr/AgNbO_3$ composite with hanced visible-light photocatalytic activity." *Applied Surface Science* 273 (2013): 159-166.

[20] Bitter, J. H., et al. "The role of the oxidic support on the deactivation of Pt catalysts during the CO_2 reforming of methane." *Catalysis Today* 29.1-4 (1996): 349-353.

[21] Edwards, J. H., and A. M. Maitra. "The chemistry of methane reforming with carbon dioxide and its current and potential applications." *Fuel Processing Technology* 42.2-3 (1995): 269-289.

[22] Li, G., et al. "Surface photoelectric properties of AgNbO3 catalyst." *Journal of Physics D: Applied Physics* 42.23 (2009): 235503.

[23] Raj, K., and B. Viswanathan. "Effect of surface area, pore volume and particle size of P25 titania on the phase transformation of anatase to rutile." *Indian Journal of Chemisty – Section A(IJC-A)* 48A (2009): 8.

[24] Nagaoka, K., K. Takanabe, and K. Aika. "Influence of the reduction temperature on catalytic activity of Co/TiO_2 (anatase-type) for high pressure dry reforming of methane." *Applied Catalysis A: General* 255.1 (2003): 13-21.

[25] Fakeeha, A. H., A. S.A. Al-Fatesh, and Ahmed E. Abasaeed. "Modification of alumina support with TiO_2-P25 in CO_2 reforming of CH_4." *Journal of Industrial and Engineering Chemistry* 18.1 (2012): 212-217.

[26] Al-Fatesh, A. S.A., A. H. Fakeeha, and A. E. Abasaeed. "Effects of promoters on methane dry reforming over Ni catalyst on a mixed (a-Al_2O_3 + TiO_2-P25) support." *International Journal of Physical Sciences* 6.36 (2011): 8083-8092.

APPENDIX A: PHOTOGRAPHS OF EQUIPMENT SETUP

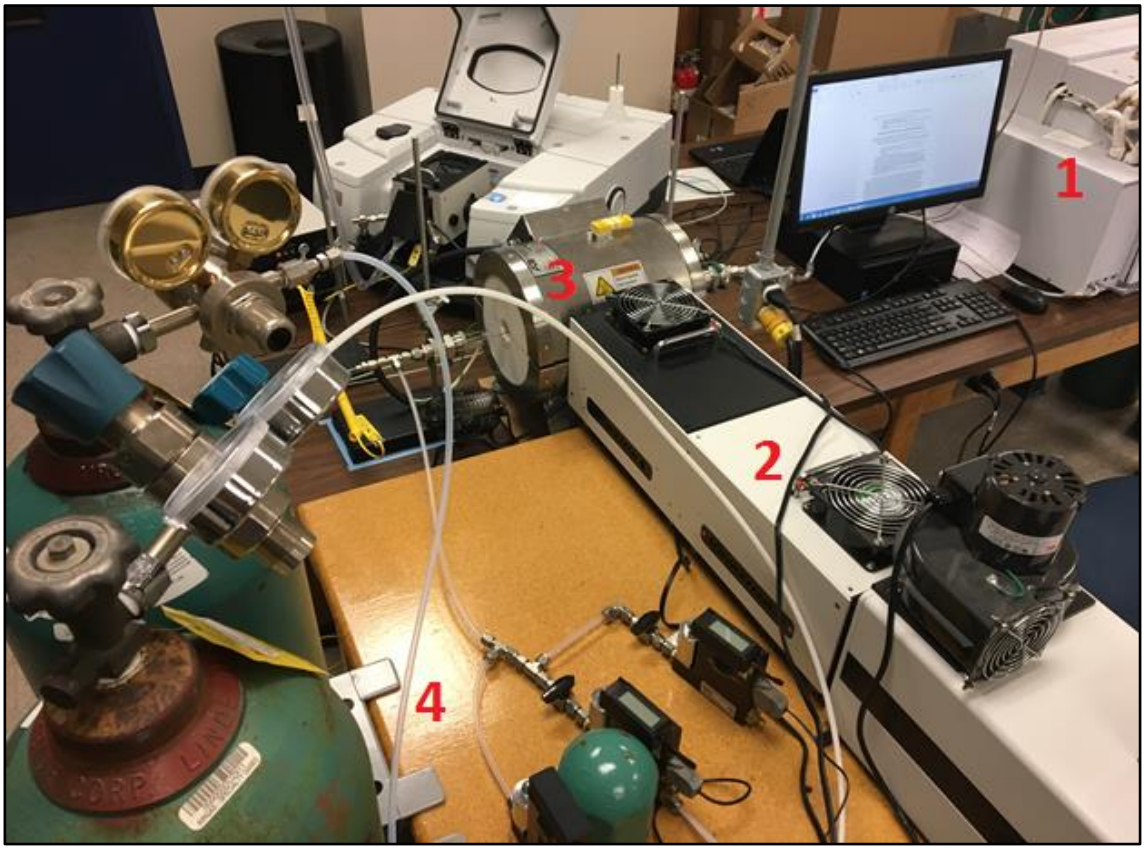

Figure 21A. Isometric view of experimental setup. Equipment components are listed as numbers 1 through 4. Item number 1 being the GC, 2 the Continuous Solar Concentrator, 3 the Split Tube Furnace, and 4 the MFCs. From this view, the spatial setup of the experiment can be appreciated.

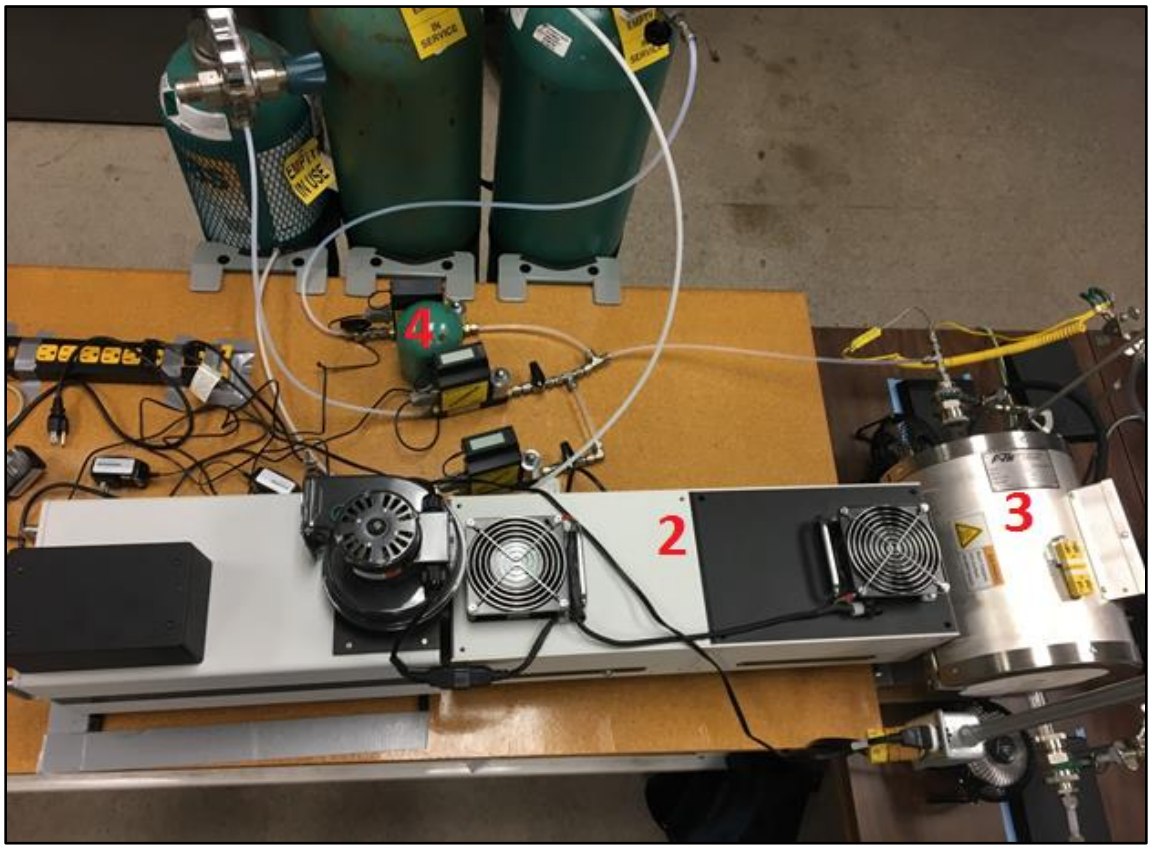

Figure 21B. Side view of experimental setup (excluding GC). Equipment components are listed as numbers 2 through 4 as the GC is not pictured here. From this view, the gas cylinders for the DRM can be seen.

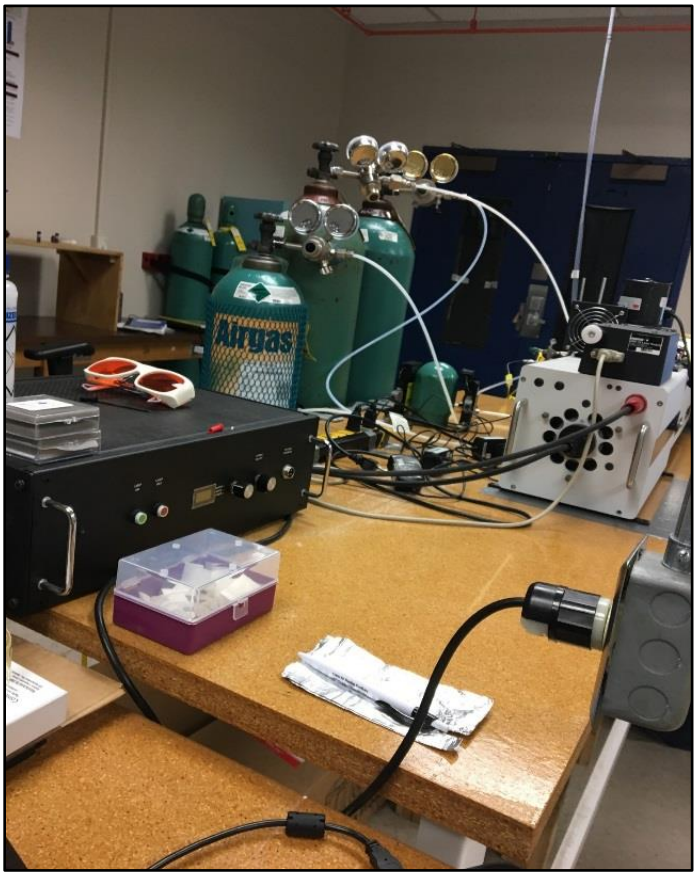

Figure 22. Rear view of experimental setup. Pictured here are the Solar Concentrator, MFCs, and Solar Power Supply. Note the holes at the base of the Lamp Housing. These are intake holes for the cooling air.

APPENDIX B: MODULAR OPTICS ENCLOSURE 1 & 2 AND FILTERS

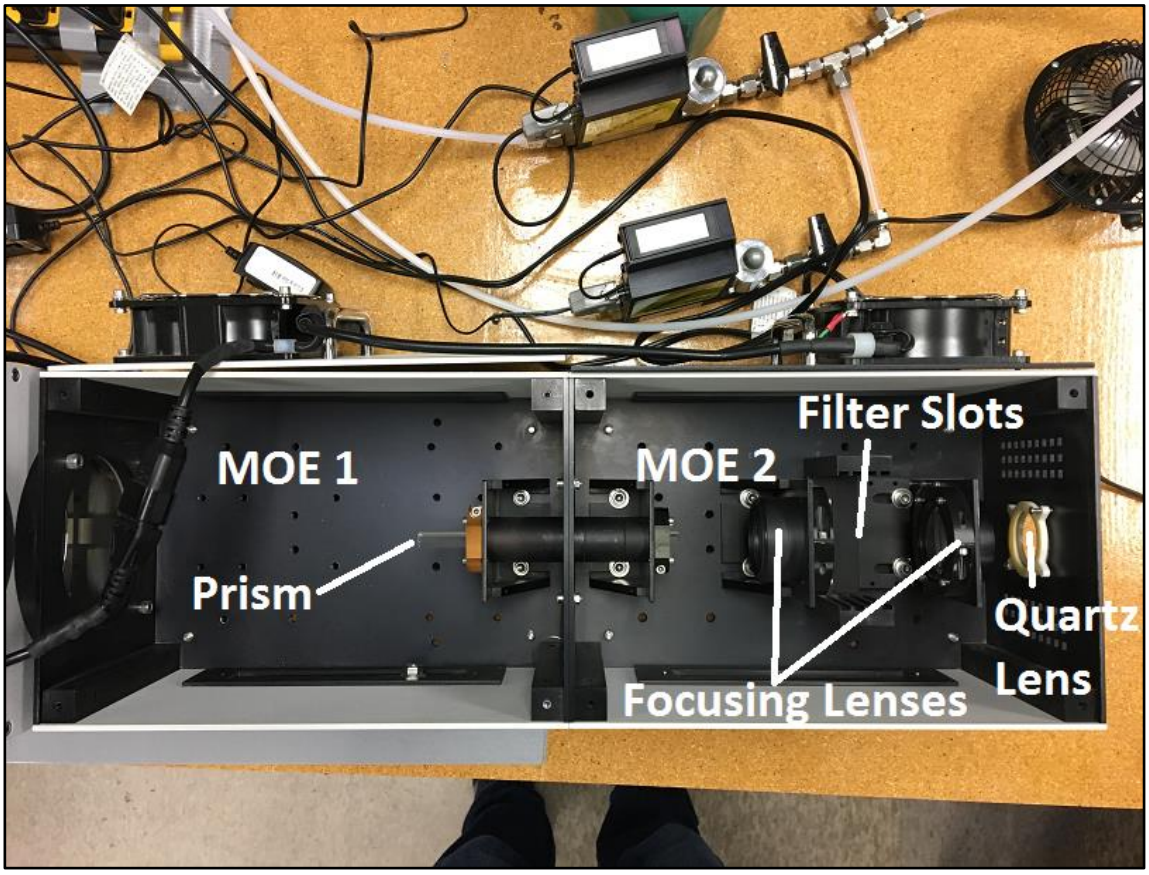

Figure 23. MOE 1 and 2 close up.

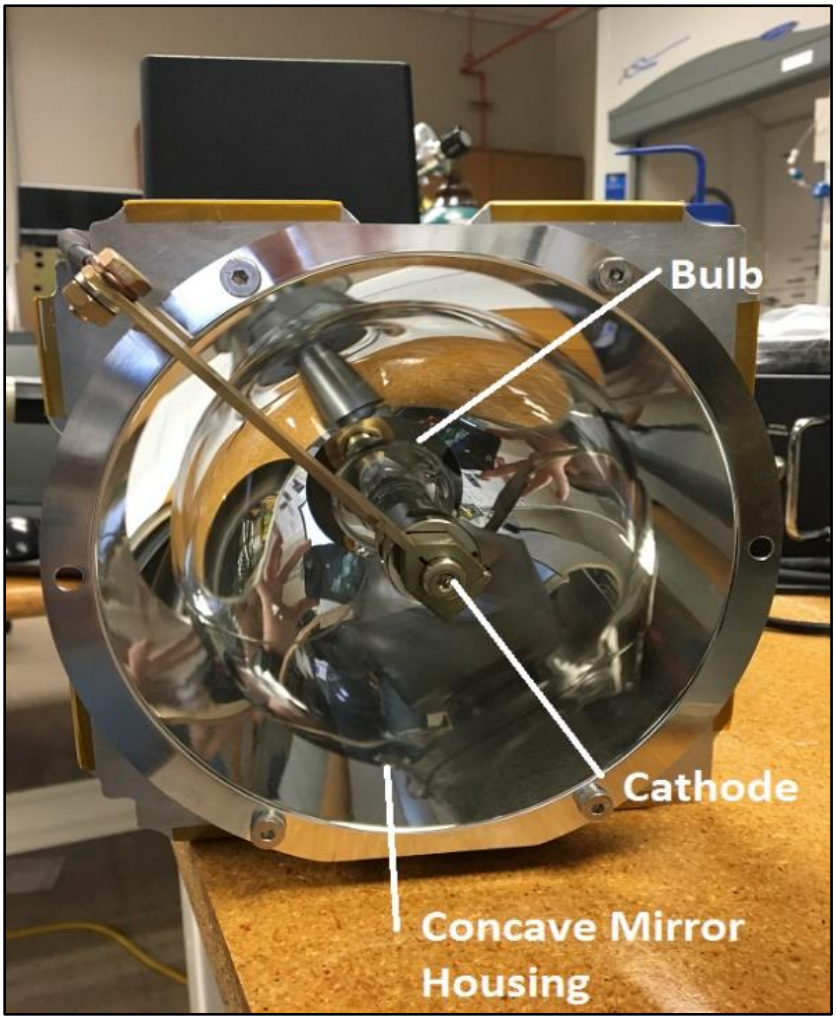

Figure 24. Concave bulb housing with cathode. In the center of the concave base, the bulb is positioned. By adjusting the depth of the bulb (Z-axis only) the intensity will be directly affected.

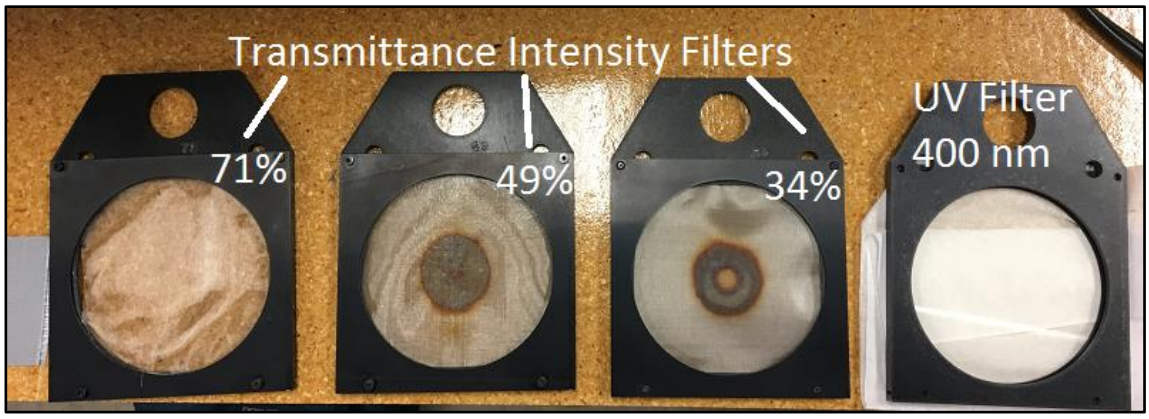

Figure 25. Transmittance Intensity and UV Filters for MOE 1. These filters allow the transmittance of the inscribed level of light intensity. Last is the UV filter which allows light with a wavelength up to 400 nm.

APPENDIX C: CONCENTRATED SOLAR PROJECTION

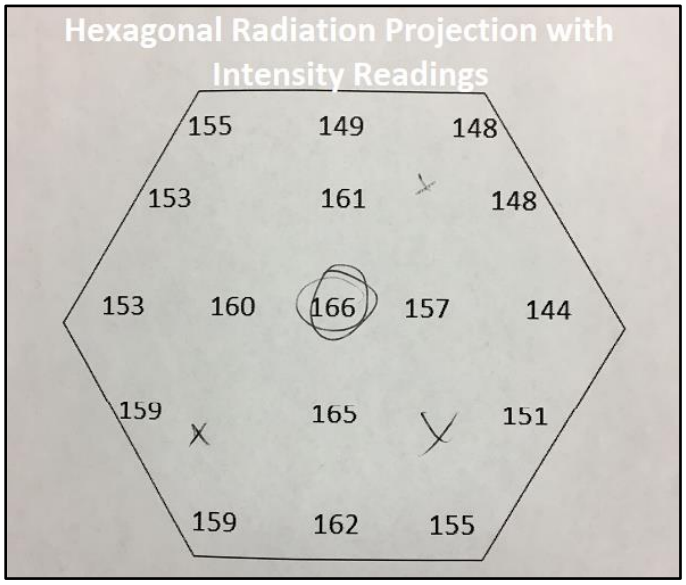

Figure 26A. Hexagonal projection of point intensity supplied by ScienceTech. Indications of intensity values were not included in literature supplied.

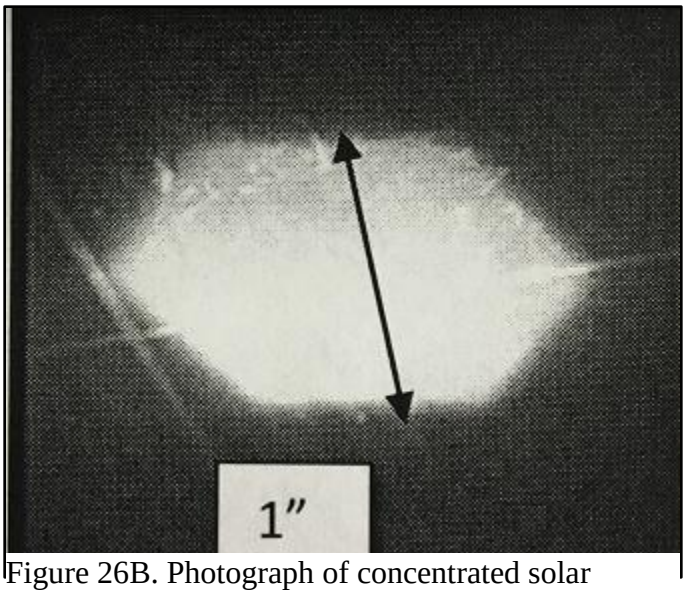

Figure 26B. Photograph of concentrated solar hexagonal projection on target. Photograph was included in literature supplied by ScienceTech.

APPENDIX D: PHOTO INTENSITY CHANGE WITH AND WITHOUT LENS

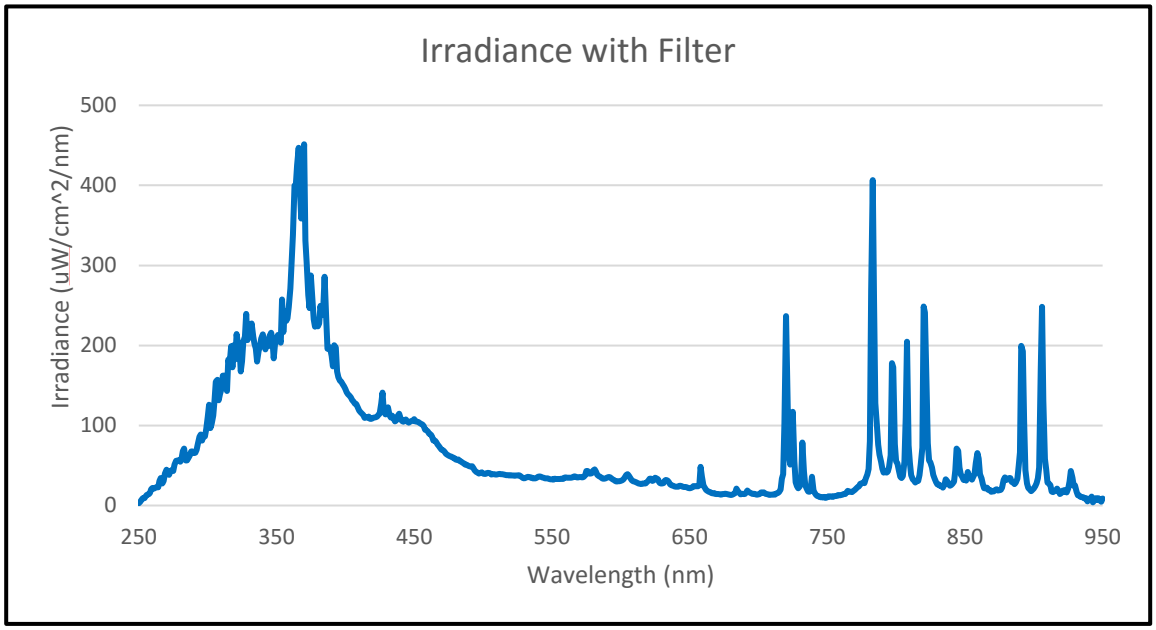

Figure 27A. Spectral Irradiance plots of Bulb #2 with Quartz lens in place. Light spectrum is full UV-IR ranging from 250-950nm. Loss of intensity due to lens is approximately 5%

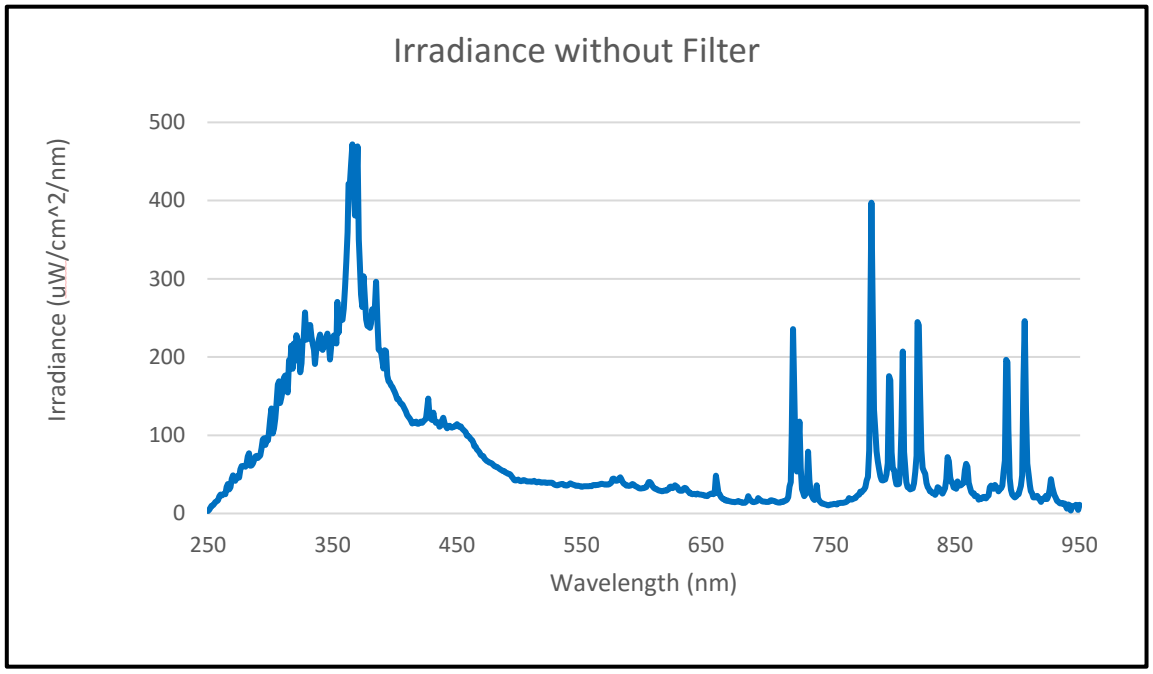

Figure 27B. Spectral Irradiance plots of Bulb #2 without Quartz lens.

APPENDIX E: QUARTZ FRIT DESIGN

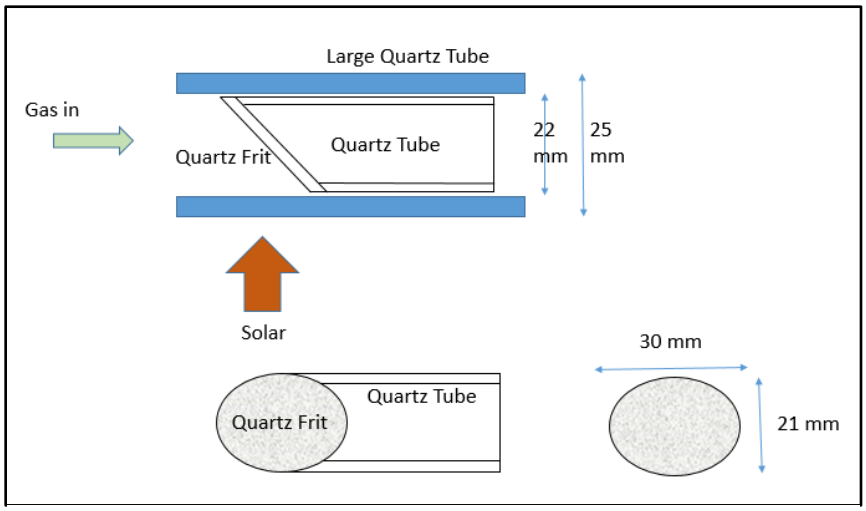

Figure 28. Schematic of Quartz tube and frit to be used as a catalyst substrate. Large quartz tube used for the reaction chamber was 22mm interior diameter and 25mm outer diameter. The small quartz tube which was fuzed with the frit had an inner diameter of 19mm and an outer diameter of 22mm. See Figure 13 for clean vs contaminated frit.

APPENDIX F: PART FAILURES

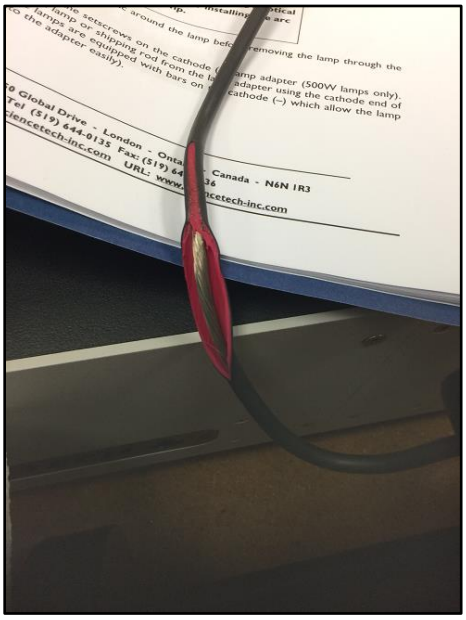

Figure 29. Splayed high amperage wire used inside lamp housing. Lamp arrived with broken wire inside. A replacement was ordered and took several weeks to arrive.

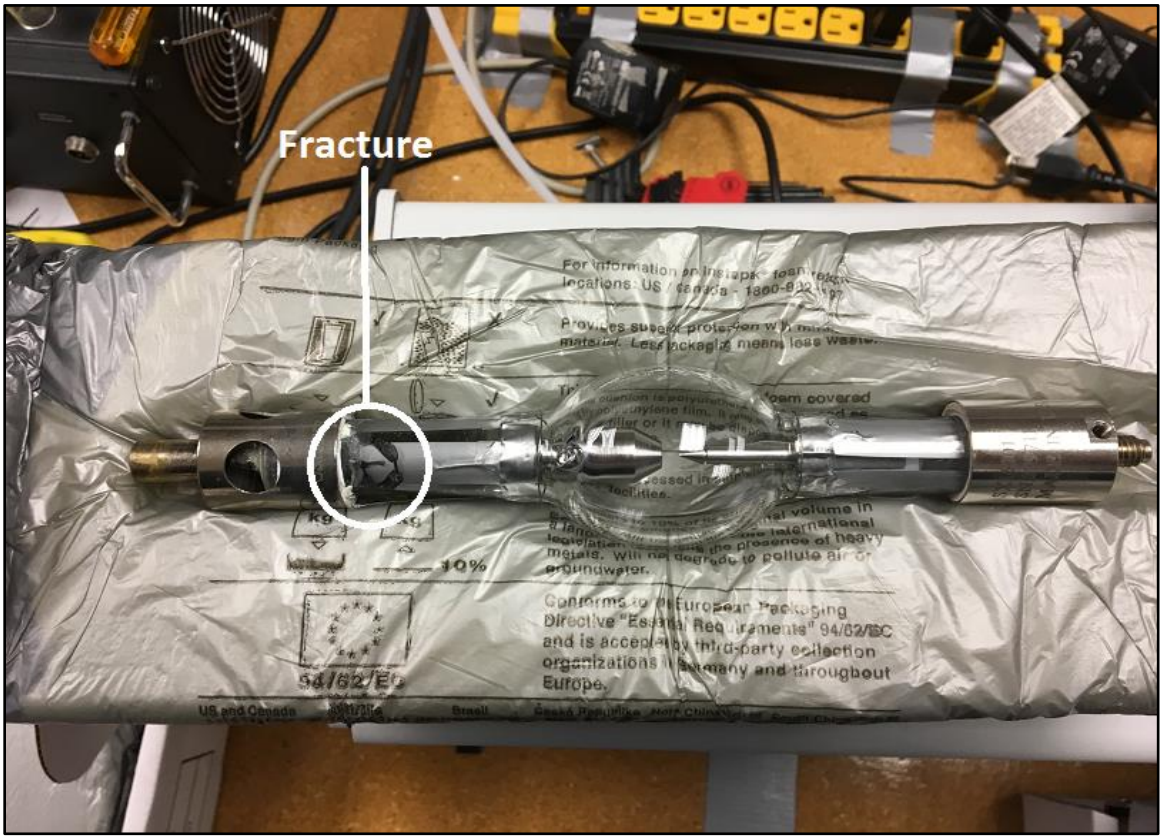

Figure 30A. Bulb #1 failure. After running at 1600W for several hours, lamp suddenly failed. Fracture near the cathode allowed xenon gas to escape. A replacement bulb was ordered and took 3 months to arrive.

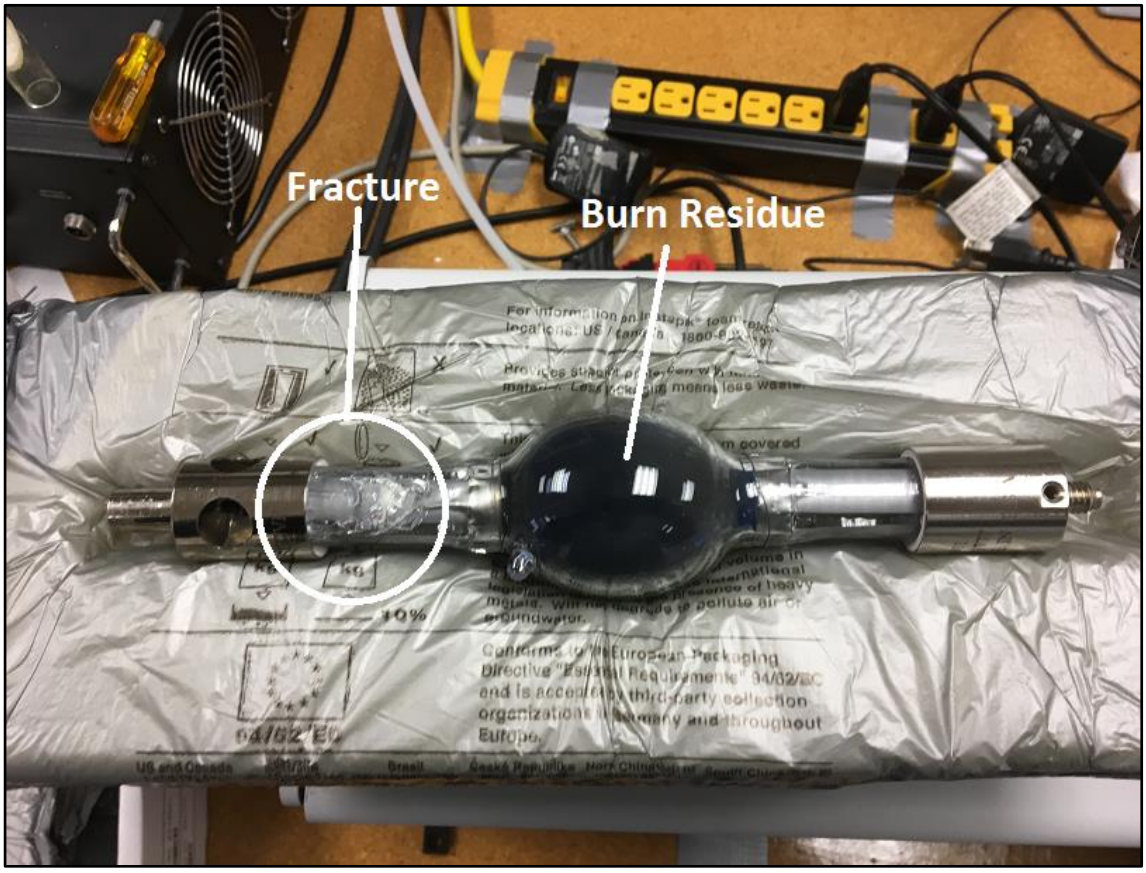

Figure 30B. Bulb #2 failure. After running at 1600W for several hours, bulb suddenly failed. Crack near cathode was similar to Bulb #1 failure. However charring of interior region between nodes indicates a combustion process. A replacement bulb was ordered and took 1 month to arrive.

APPENDIX G: IN SITU REDUCED PT-AGNBO$_3$ EXPERIMENT 1:

TESTS 1, 2 AND 3

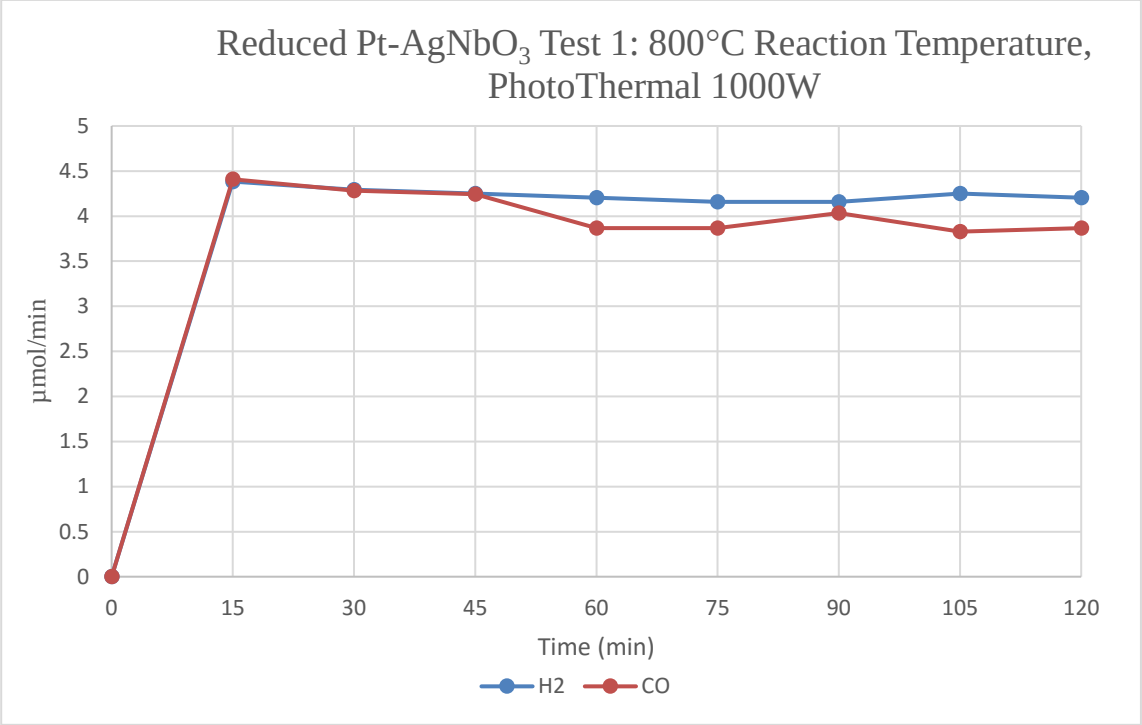

Figure 31A. Pt-AgNbO$_3$, Reduced DRM Test 2 with 20 mg Pt- AgNbO$_3$, Reduced *In Situ* with 5 mL/min H_2 and 45 mL/min Ar at 500°C for 1 hr, exposed to 10 mL/min of 10% CO_2 / 10% CH_4 / Ar gas at a reaction temperature of 800°C.

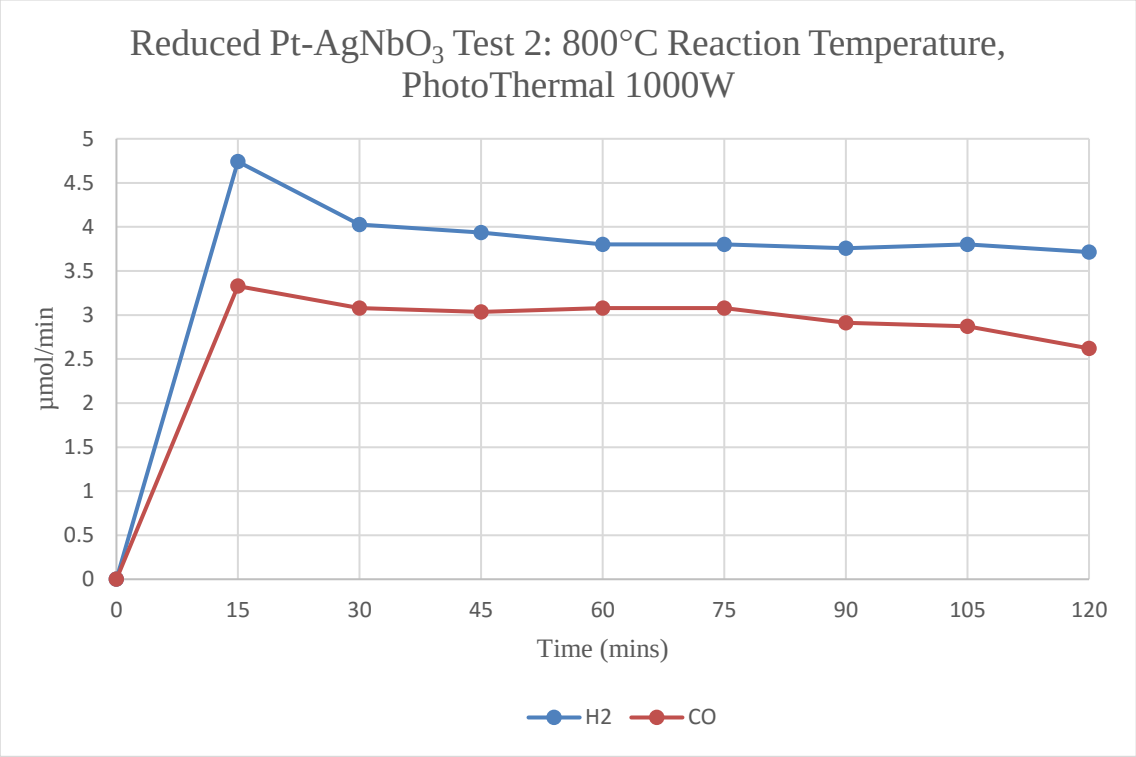

Figure 31B. Pt-$AgNbO_3$, Reduced DRM Test 2 with 20 mg Pt-$AgNbO_3$, Reduced *In Situ* with 5 mL/min H_2 and 45 mL/min Ar at 500°C for 1 hr, exposed to 10 mL/min of 10% CO_2/ 10% CH_4 / Ar gas at a reaction temperature of 800°C.

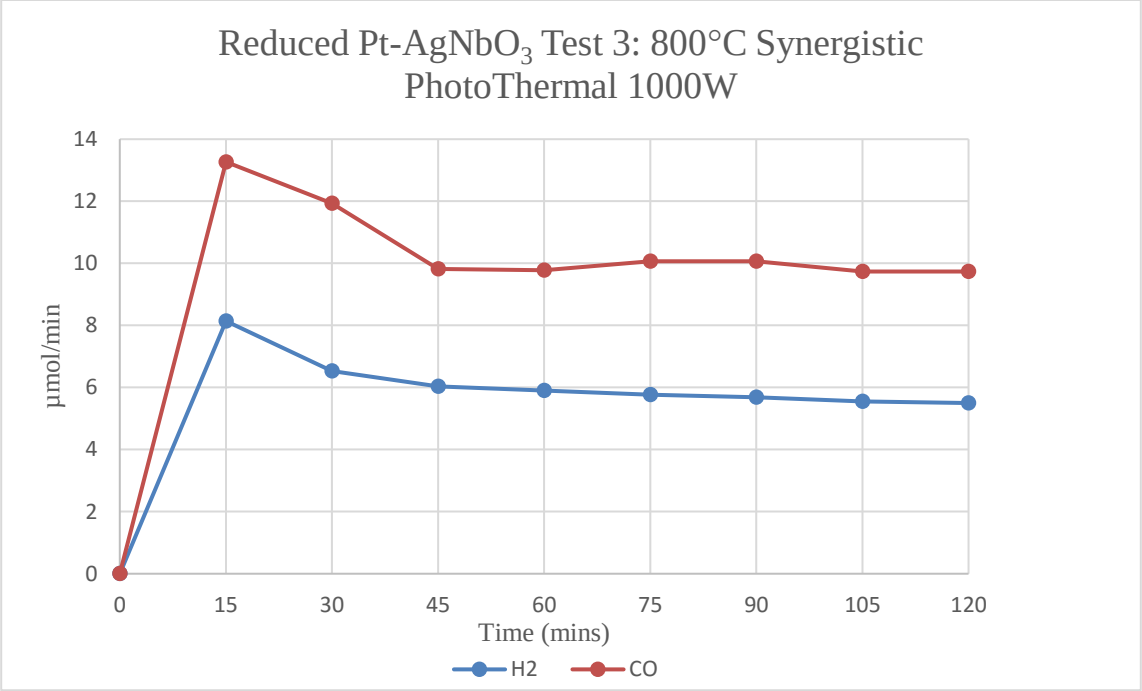

Figure 31C. Pt-$AgNbO_3$, Reduced DRM Test 3 with 20 mg Pt-$AgNbO_3$, Reduced *In Situ* with 5 mL/min H_2 and 45 mL/min Ar at 500°C for 1 hr, exposed to 10 mL/min of 10% CO_2 / 10% CH_4 / Ar gas at a reaction temperature of 800°C. This differs from previous tests and the quantities of production are ~3x higher than the other two tests.